

# NAVAL POSTGRADUATE SCHOOL

## Monterey, California



### Evaluation of the Mechanical Properties of Countermine Boots

by

Richard C. Muschek  
Quinten M. King  
Young W. Kwon

July 1, 1997-November 15, 1997

Approved for public release; distribution is unlimited.

**DTIC QUALITY INSPECTED 4**

Prepared for: United States Marine Corps Systems Command  
Quantico, Virginia 22134-5010

19980102 100


Naval Postgraduate School  
Monterey, California

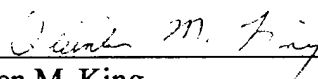
Rear Admiral M. J. Evans  
Superintendent


R. S. Elster  
Provost

This report was prepared in conjunction with research conducted for the United States Marine Corps Systems Command.

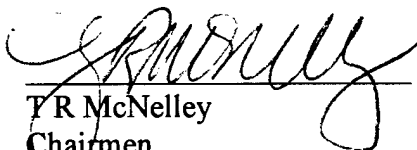
This report was prepared by:

  
Richard C. Muschek  
CPT, USA

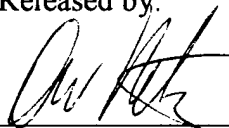
  
Quinten M. King  
LT, USN

  
Young W. Kwon  
Associate Professor of Mechanical Engineering

Reviewed by:

  
T R McNelley  
Chairman  
Dept. of Mechanical Engineering

Released by:

  
D W Netzer  
Dean of Research

<b>REPORT DOCUMENTATION PAGE</b>			<b>Form Approved OMB No. 0704-0188</b>	
Public reporting burden for this collection of information is estimated to average 1 hour per response, including the time for reviewing instructions, searching existing data sources, gathering and maintaining the data needed, and completing and reviewing the collection of information. Send comments regarding this burden estimate or any other aspect of this collection of information, including suggestions for reducing this burden to Washington headquarters Services, Directorate for Information Operations and Reports, 1215 Jefferson Davis Highway, Suite 1204, Arlington VA, 22202-4302, and to the Office of Management and Budget, Paperwork Reduction Project (0704-0188), Washington DC, 20503.				
<b>1. AGENCY USE ONLY</b>		<b>2. REPORT DATE</b> November 15, 1997		<b>3. REPORT TYPE AND DATES COVERED</b> Final Report 7/97 to 11/97
<b>4. TITLE AND SUBTITLE</b> Evaluation of the Mechanical Properties of Countermine Boots			<b>5. FUNDING NUMBERS</b>  N9545097WRR7AVS	
<b>6. AUTHORS</b> Richard C. Muschek, Quinten M. King, Young W. Kwon				
<b>7. PERFORMING ORGANIZATION NAME AND ADDRESS</b> Naval Postgraduate School Monterey, CA, 93943			<b>8. PERFORMING ORGANIZATION REPORT NUMBER</b> NPS-ME-97-007	
<b>9. SPONSORING/MONITORING AGENCY NAME AND ADDRESS</b> United States Marine Corps Systems Command			<b>10. SPONSORING/MONITORING AGENCY REPORT NUMBER</b>	
<b>11. SUPPLEMENTARY NOTES</b> The views expressed in this report are those of the authors and do not reflect the official policy or position of the Department of Defense or the U.S. Government				
<b>12a. DISTRIBUTION/AVAILABILITY STATEMENT</b> Approved for public release; distribution is unlimited			<b>12b. DISTRIBUTION CODE</b> A	
<b>12. ABSTRACT</b> (Maximum of 200 words) The goal of this project was to test the mechanical properties of countermine boots and overboots which are currently available for U.S. soldiers. The soles of both boots were made of almost the same materials and the same layout of the materials. The used materials were a rubber, an aluminum honeycomb, a stainless steel, and a kevlar composite. The kevlar composite had different properties for the countermine boot and overboot, respectively. The major structural strength and stiffness of the boots came from the aluminum honeycomb with stainless steel faceplates. All the materials used in the boots' soles were tested using an uniaxial testing machine called Instron to determine their mechanical material properties like elastic moduli and ultimate strengths. Further, the Scanning Electron Microscopy (SEM) was used for the stainless steel material to determine their chemical compositions. All the tests were conducted for multiple specimens to ensure their properties. The material data were tabulated and the stress-strain curves were attached in this report. Further, a preliminary finite element analysis was conducted to evaluate the countermine boot against an anti-personnel mine such as the M-14 mine.				
<b>14. SUBJECT TERMS</b> Finite Element Method, Material Properties, Mechanical Testing			<b>15. NUMBER OF PAGES</b> 93	
			<b>16. PRICE CODE</b>	
<b>17. SECURITY CLASSIFICATION OF REPORT</b> Unclassified	<b>18. SECURITY CLASSIFICATION OF THIS PAGE</b> Unclassified	<b>19. SECURITY CLASSIFICATION OF ABSTRACT</b> Unclassified	<b>20. LIMITATION OF ABSTRACT</b> UN	

## ABSTRACT

The goal of this project was to test the mechanical properties of countermine boots and overboots which are currently available for U.S. soldiers. The soles of both boots were made of almost the same materials and the same layout of the materials. The used materials were a rubber, an aluminum honeycomb, a stainless steel, and a kevlar composite. The kevlar composite had different sizes of woven fibers for the countermine boot and overboot, respectively. The major structural strength and stiffness of the boots were the aluminum honeycomb with stainless steel faceplates.

All the materials used in the boots' soles were tested using an uniaxial testing machine called Instron to determine their mechanical material properties like elastic moduli and ultimate strengths. Further, the Scanning Electron Microscopy (SEM) was used for the stainless steel material to determine their chemical compositions. All the tests were conducted for multiple specimens to check their repeatability. The material data were tabulated and the stress-strain curves were attached in this report.

Further, a preliminary finite element analysis was conducted to evaluate the countermine boot against an anti-personnel mine such as the M-14 mine.

## TABLE OF CONTENTS

1. INTRODUCTION AND BACKGROUND	1
2. CLASSIFICATION OF ANTI-PERSONNEL MINES	3
3. EXPLOSIVE CHARACTERISTICS OF ANTI-PERSONNEL MINES	5
4. PROJECT GOAL	9
5. SPECIMEN PREPARATION AND TEST PROCEDURE	11
5.a. Rubber	11
5.b. Aluminum Honeycomb	13
5.c. Stainless Steel	14
5.d. Kevlar	16
6. TEST RESULTS	21
6.a. Rubber	21
6.b. Aluminum Honeycomb	22
6.c. Stainless Steel	22
6.d. Kevlar	24
7. FINITE ELEMENT MODEL	29
8. BLAST EFFECTS ON COUNTERMINE BOOTS	35
9. BLAST EFFECTS ON THE LOWER EXTREMITIES	45
10. CONCLUSIONS	59
LIST OF REFERENCES	61
APPENDIX A: MICROANALYSIS OF STEEL SHANK	65
APPENDIX B: STRESS VS STRAIN CURVES OF RUBBER SPECIMENS	69
APPENDIX C: STRESS VS STRAIN CURVES OF HONEYCOMB SPEC.	75
APPENDIX D: STRESS VS STRAIN CURVES OF STEEL SPECIMENS	79
APPENDIX E: STRESS VS STRAIN CURVES OF KEVLAR SPECIMENS	81
APPENDIX F: ELEMENT LOCATIONS IN THE FEM.	85
INITIAL DISTRIBUTION LIST	93

## 1. INTRODUCTION AND BACKGROUND

During the World War I, the emergence of the main battle tank spurred the development of the Anti-Tank Mine (AT Mine). These first AT mines were clumsy and ill conceived, being easily redeployed by opposing forces. Between World Wars a tremendous effort was mounted to develop the Anti-Personnel Mine (AP Mine) to protect these AT Mines. Leading military strategists in particular those in Eastern Europe began to see ways to expand the AP Mines role in conventional warfare. They accomplished this by linking the mine to the protection of specific military targets and aimed at enemy soldiers.

After World War II, mines grew not only in popularity but also in sophistication. Hundreds of different types as well as variations sprung up making detection and disposal significantly more difficult. During the 1960's a new dangerous application for land mines began to advance. During a nine year bombing campaign of Laos, thousands of mines were air dropped indiscriminately in an attempt to close the Ho Chi Minh trail. This trend continued during Cambodia's civil war. Opposing factions scattered even more mines randomly throughout the country. No side kept records of where or how many mines they deployed. By the end of the war, more people were killed by AP Mines than by any other armament [1].

When the Soviets invaded Afghanistan in 1979, randomly targeted and remotely deployed minefields had become a viable and acceptable part of military doctrine. Cheap as well as easy to

produce and deploy Land Mines have become an economical force equalizer for many third world countries. Forces attempting to move against random minefields lose not only mobility on the battlefield, but also must expend critical assets to clear maneuvering lanes.

Mines also create a psychological advantage as the opposing forces become much more pensive and thoughtful before advancing. AP Mines tend to maim and injure soldiers rather than kill. This creates a significant strain on the logistical and medical capabilities of the advancing force.

Today an estimated 110 million AP mines are thought to be deployed around the world with another 100 million in stock-piles ready for use. With an additional 5 to 10 million being produced annually, AP Mines will continue to remain a significant threat to military personnel and the civilian community well into the future.

The US made M-14 AP Mine is typical in explosive charge and weight. Its design has been copied and used in many other countries as well [1, 2]. This study will use this mine as a standard to measure the effectiveness of the countermine boot against injury of the lower extremity of a soldier.

## 2. CLASSIFICATION OF AP MINES

To fully appreciate the requirements needed for protective footwear we must first understand the nature of the Anti-Personnel Mines. AP Mines are generally classified into two main groups: Blast and Fragmentation Mines. Fragmentation mines are designed to hurl shrapnel at the legs and torso of approaching soldiers. Footwear is generally not designed to provide protection against this type of threat. Blast mines are designed to cause injury and maiming by subjecting the lower extremities to blast waves. The detonation creates large over pressures and impulses that are transmitted axially to the lower extremities. It is believed proper engineering design of footwear can significantly reduce the damage inflicted by this type of mine.

The M-14 AP mine is one of the most common mines and it was originally developed in the United States and has been produced under license in the US, India, and Vietnam [2]. Several other countries produce several copycat versions throughout the world. It has a simple pressure switch actuator requiring approximately 20 pounds of weight to initiate. Its plastic body and small size makes detection difficult even in the best of conditions. The only metal in this mine is a small steel striker tip. This mine utilizes a main explosive charge of 1 ounce of Teteryl (an equivalent of 1.07 ounces of TNT). The present finite element analysis used the M-14 AP mine against a countermining boot.





### 3. EXPLOSIVE CHARACTERISTICS OF AP MINES

When an explosive mine is detonated, it creates a hemispherical blast wave. This blast wave is generated when the atmosphere surrounding the explosion is forcibly pushed back by the gases produced from the chemical reaction of the explosive [3]. This wave can be illustrated in Figure 3-1. This overpressure can be calculated using Equations 3.1 and 3.2 [3]

$$\frac{p_o}{p} = \frac{808 * \left[ 1 + \left( \frac{Z}{4.5} \right)^2 \right]}{\sqrt{1 + \left( \frac{Z}{0.048} \right)^2} * \sqrt{1 + \left( \frac{Z}{0.32} \right)^2} * \sqrt{1 + \left( \frac{Z}{1.35} \right)^2}} \quad \text{Eqn 3.1}$$

where

$$Z = \frac{d * f_d^{\frac{1}{3}}}{W^{\frac{1}{3}}} \quad \text{Eqn 3.2}$$

The left hand side term of Equation 3.1 is the ratio of the explosion over-pressure to the ambient atmospheric pressure and Z is the scaled distance from the detonation point. In Equation 3.2, d is the distance from the blast in meters,  $f_d$  is the transmission factor of atmospheric density, and W is the scaled weight of the explosive. All constants are calculated for metric units.

Scaling values are used to help make comparisons between similar events. These scaling relations are derived from the

same Buckingham PI Theorem that helps Aeronautical Engineers build a scale model and use it to predict behavior of the actual jet. In the present case, the scaled distance relates the actual distance, atmospheric density, and the energy released from the chemical reaction of the explosive.

The cube root values are derived from the geometrical similarity based for a spherical blast. Due to the relatively small amounts of explosives and distances involved, it may be assumed the atmospheric density is homogeneous and uniform through out the area of interest.

Also of importance is determining the duration of the blast. The amount of energy dissipated over time gives a good indication of the damage causing potential of the blast. A fixed amount of energy dissipated over a longer time will cause less damage than that same amount dissipated quickly. The duration of the blast is considered to be the length of time for which the positive pressure wave exists. For a chemical explosion, this can be calculated using Equation 3.3 [3]

$$\frac{T_d}{W^{\frac{1}{3}}} = \frac{980 * \left[ 1 + \left( \frac{Z}{0.54} \right)^{10} \right]}{\left[ 1 + \left( \frac{Z}{0.02} \right)^3 \right] * \left[ 1 + \left( \frac{Z}{0.74} \right)^6 \right] * \sqrt{1 + \left( \frac{Z}{6.9} \right)^2}} \quad \text{Eqn 3.3}$$

where  $t_d/W^{1/3}$  is the duration in milliseconds for a one kilogram TNT explosion in standard atmospheric pressure.  $Z$  is the scaled distance as defined above.

For small yield explosions of short duration like those encountered in the case of AP mines, the impulse delivered by the blast is often the leading contributor to the damage causing ability of the explosion. Impulse can best be visualized as the area under the pressure-time curve. As with the duration of the blast, the significant portion of the impulse is contained under the positive pressure phase of the blast. This portion is then indicative of the entire impulse characteristic of the entire blast wave. The impulse per unit area can be calculated using Equation 3.4 [3].

$$\frac{I}{A} = \frac{0.067 * \sqrt{1 + \left(\frac{Z}{0.23}\right)^4}}{Z^2 * \left[1 + \left(\frac{Z}{1.55}\right)^3\right]^{\frac{1}{3}}} \quad \text{Eqn 3.4}$$

Blast wave impulse depends not only on the peak overpressure and the wave duration, but also on the rate of decay of the overpressure. The slower the decay, the greater the area under the curve, thus the greater the impulse provided. This can best be seen in Figure 3-2. This figure shows how the blast wave from a typical nuclear explosion (curve A) decays faster and shows a smaller impulse per unit area than one from a chemical explosion (curve B) even though their durations and peak overpressures are identical.

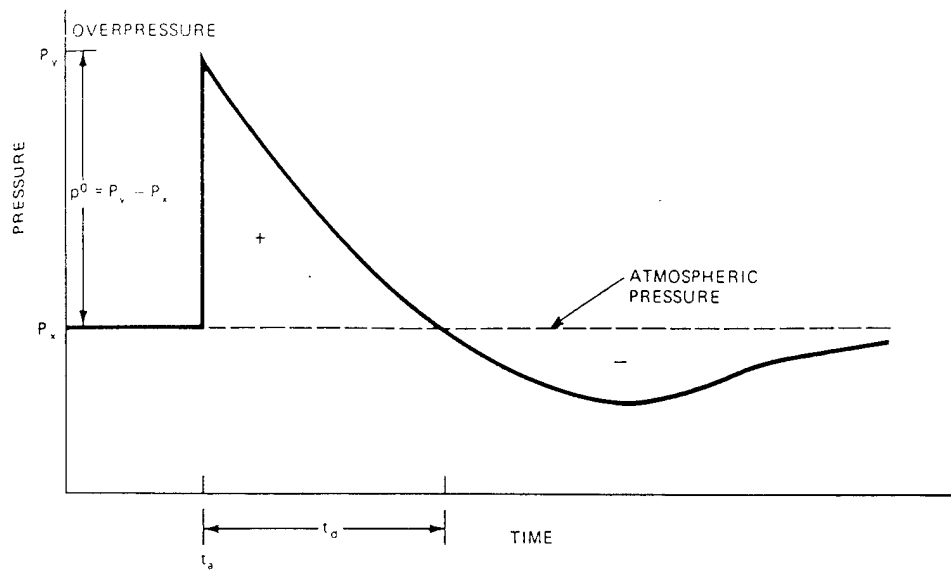


Figure 3-1: Pressure vs time curve for a blast wave. [3]

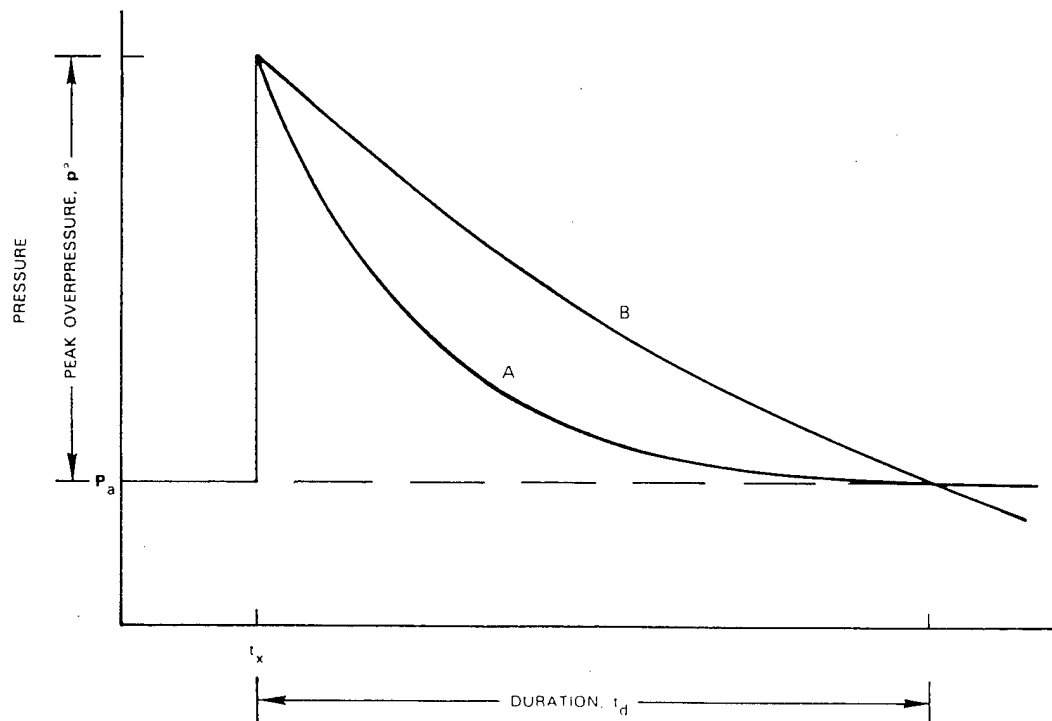


Figure 3-2: Pressure vs time curve comparison. Curve A is a typical nuclear explosion and curve B is a typical chemical explosion. [3]

#### 4. PROJECT GOAL

The goal of this project was to determine the mechanical properties of the materials used in the countermine boot and the overboot. In order to achieve the goal, test specimens were prepared from the already manufactured boots. Because of this, there were some limitations in the specimen geometries as well as in the testing. Instron, a uniaxial testing machine, was used for the mechanical testing and the Scanning Electron Microscopy (SEM) was used to find the chemical compositions of the material that turned out to be a stainless steel.

Because of limited budget and scope during this project, a live fire testing of the boots with cadaver limbs could not be performed. Instead, a finite element analysis was conducted to determine the effectiveness of the countermine boot against the lower limb injury when the boot was subjected to the M-14 AP mine.

This analysis is preliminary because it should be further validated from a live fire testing with a cadaver limb. Some of parameters used in the analysis would not be validated otherwise. Therefore, the analysis results were not conclusive but provide some useful information.



## 5. SPECIMEN PREPARATION AND TEST PROCEDURE

As mentioned previously, the amount of material to be used as a test specimen was limited in both quantity and shape to that used in each boot. The American Society of Testing Materials (ASTM) [4] publishes accepted standards for testing all involved materials in different ways to get different properties. The ASTM standards for specimen dimensions were adhered to as much as possible for the available material. Wherever dimensions and/or test procedures vary from the ASTM is addressed below.

### 5.a. Rubber

Specimen Preparation: Due to the available shape of the rubber to be tested (the sole of a boot), testing the rubber in tension was not an option because the bar shaped test specimen required in the ASTM needs more rubber than was available. (See ASTM D412-92 specifications for recommended bar dimensions [5].) In addition, shaping the specimen from a rubber already in its final form requires extensive tooling in a machine shop. It was recognized that cutting rubber specimens to precision was difficult [6]. Also, the common applications of the rubber used in the sole of a boot are more compressive in nature. Therefore, it was decided to gather properties for the rubber via compressive tests. ASTM D575-91, Standard Test Methods for Rubber Properties in Compression [7], specifies the dimensions of test specimens as 1.129 inch in diameter and 0.49 inch in thickness. Given the available contour and thickness of the boot



sole, it was obvious that these dimensions were not possible. Therefore, it was determined to use the same ratio of diameter to thickness, 2.3 to 1.0, with smaller sized test specimens. The proper specimen size was 0.39 inch diameter and 0.17 inch thick. (See Figure 5-1.) These specimens were milled out using a die fabricated in a machine shop to duplicate recommendations of ASTM D575. The die was placed in a drill press and lubricated with soapy water so that a smooth cut could be obtained. The cutting pressure was kept sufficiently low to avoid "cupping" of the cut surface. The specimens were then cut to the appropriate thickness using a very sharp bladed apparatus used in the construction of delicate models.

Test Procedure: The test procedure for the rubber specimens involved applying a constant crosshead speed as a compressive force compresses the cylindrically-shaped specimens. In accordance with ASTM D575, after measuring the exact dimensions of the specimen, each specimen was placed between the crossheads of the testing machine. Sheets of 400 Grit waterproof sandpaper were placed between the specimens and the machine surface to resist lateral slippage. (This Grit of sandpaper is also recommended by the ASTM D575.) In accordance with ASTM D575, a continual force was applied at a rate of 0.5 in/min until the desired deflection was achieved. For these tests, compression was continued until the grips of the machine nearly contacted one another. This test procedure was repeated for three different rubber specimens from two separate boots for a total of six specimens.

The Instron machine automatically recorded and stored the load and deflection data that was then downloaded as an ASCII file. This data was then transferred to a MATLAB program. The use of MATLAB eased the manipulation of the raw data for the calculation of strength values, Young's moduli of elasticity, etc, and plotting. This transfer of data via an ASCII file to MATLAB was followed for the data collected for all the test materials.

#### 5.b. Aluminum Honeycomb

Specimen Preparation: The honeycomb specimen dimensions were also limited by the shape and amount of honeycomb available in each shank. Since testing of the honeycomb was to be conducted to determine the properties in three directions<sup>1</sup>, it was desirable to have the shape of all specimens as uniform as possible. A rectangular prism specimen allowed for maximum use of available raw material. Given the shape of the shank, it was determined that 0.9 in x 0.9 in x 0.5 in specimens would optimize the available material for test specimens. (See Figure 5-2.) These shapes were cut on a saw in a machine shop at a very slow rate and with minimal clamping pressure. It was found that application of too much clamping pressure on the honeycomb caused the bonding between the aluminum sheets to separate. Honeycomb

---

<sup>1</sup> *Compressive direction* was the direction downward on the sole. *Ribbon direction* (longitudinal direction) was the direction in which the sheets of aluminum ran. [heel-to-toe] *Transverse direction* was the direction in which the aluminum sheets were bonded. [side-to-side on the foot]

from three different shanks were cut to get three uniform specimens from each shank. Two of the shanks came from countermine boots and the other shank came from of a countermine overboot.

Test Procedure: The test procedure was to gather compressive material properties on the honeycomb. The honeycomb was compressed on all three axes (that is, in all three directions). Each sample was compressed beyond the point at which the honeycomb failed and was continued until the honeycomb became nearly solid. Stopping the test at this point seemed prudent since all useful data was obtained early in the test and continuing the test risked damage to the Instron machine.

#### **5.c. Stainless Steel**

Specimen Preparation: The stainless steel used on the top of the shank was considerably thinner than that used as the bottom of the shank, 0.02 in versus 0.06 in. ASTM E8-96, Standard Test Methods for Tension Testing of Metallic Materials [8], specifies the standard "dog bone" shape to be used depending upon the thickness of the material. It was recognized that precise specimen preparation would be difficult with very thin samples. Acknowledging that the top piece of steel was thin, it was determined that if both steels were proven to be the same only the thicker steel would have to be cut and tested to find the material properties of both. With the Scanning Electron Microscope (SEM) and the Energy-Dispersive X-ray (EDX) machine,

this was proven to be the case. (See Appendix A for this procedure and discussion of results.)

With only the thicker steel to test, the next task was to determine the dimensions of the sample. As was the case with the rubber, the ASTM required more material than was available. Therefore, the dimension were again scaled proportionally and cut using an Electrical Discharge Machine (EDM)<sup>2</sup> to ensure accuracy. The dimensions used can be seen in Figure 5-3. Three of these specimens were cut. One was from one blast boot and the other two were from the same shank in a different blast boot.

Test Procedure: This test was to gather tensile material properties of the specimens. The test procedure outlined in E8-96 is very specific on the procedure depending upon desired data, gauge length of the specimen, size of extensometer, etc. One concern was possible slippage in the grips since the specimen, while thicker than the top steel, was still a relatively thin sample. Therefore, each specimen was cleaned with acetone to ensure the removal of all epoxy and rubber residue left from the removal from the boot. The specimens were then placed in common wedge-shaped grips in the Instron machine. This wedge shape is designed to encourage a tight grip as force is applied and extension, as well as thinning, of the specimen occurs. Given

---

<sup>2</sup> *Background on the EDM:* The EDM is often used to cut high strength, electrically conductive materials to precision. The fundamental process of the machine is to use flowing, electrically charged water to induce an electrical charge in the material. An electrically charged, moving wire then cuts through the material along the desired path at a very slow rate. While passing through the material, this thin wire is essentially melting the material and cutting out the desired/ programmed shape. The code used to program the EDM is a simple DOS-based code.

the expected high strength of the steel, an extensometer was attached to the specimen to ensure accurate readings of initial displacement. (While the Instron machine is accurate at obtaining data, using an extensometer to gather the data in tensile tests is more accurate.) In accordance with ASTM E8-96, an extensometer with a gauge length smaller than the gauge length of the specimen was selected, 0.5 vs 0.8 inch, respectively.

The cross-head speed recommended by ASTM E8-96 correlates to a strain rate between 0.05 in/in/min and 0.5 in/in/min. Given the dimensions of these specimens, a strain rate of just under 0.5 in/in/min equated to a cross-head speed of 0.05 in/min. Due to limitations on the extensometer used, data collection switched from the extensometer to the Instron machine at 4% strain. This proved to work out quite well and the extensometer was able to record data beyond the point at which the yield stress was reached. The testing was continued until failure of the specimens occurred.

#### **5.d. Kevlar**

Specimen Preparation: Testing for material properties of the kevlar was expected to be the most difficult. With no information on the type, weave, or size of the fibers, no information on the resin used, and no accurate way of counting the number of layers of the weave, there was essentially no way of calculating properties of the kevlar using common equations used for orthotropic composites. Therefore, macrotesting was the only way to get the desired properties. In ASTM D3039/D3039-95a,

Standard Test Method for Tensile Properties of Polymer Matrix Composites Materials [9], recommended dimensions of test specimens. Again, however, the ASTM dimensions for test specimens had to be scaled proportionally to accommodate the available material using desired gauge lengths as a basis. Given the limited dimensions of the material, gauge lengths of 0.75 in and 1.5 in were established for the transverse and longitudinal test specimens, respectively. Test specimens to be used for testing of transverse properties were 0.25 in wide. Test specimens for testing longitudinal properties were proportional and 0.5 in wide. The reason these width dimensions varied was to ensure an adequate number of test specimens (three) in each direction given the shape of the sole and the required overall length of the specimens based on the scaled ASTM dimensions. Grip lengths were also a concern since it was a concern that the specimens could slip in the grips. The dimension listed in Figure 5-4 allowed for grip lengths of 1.475 in and 2.0 in for transverse and longitudinal test specimens, respectively. The specimens were cut along the seams of the kevlar fabric since the seams of the fabric are longitudinal and transverse when the liner is placed in the boot.

*Gripping/Use of Tabs:* Many material configurations such as multi-directional laminates and fabric-based composites cannot be successfully tested without tabs. The use of tabs prevents stress concentrations from developing at the machine grips. This concentration of stress may cause the specimen to fail at the grips rather than in the test region. The ASTM further

recommends their use when testing unidirectional materials to failure when slippage in the grips occurs. A table provided in ASTM 3039/3039M lists tab dimensions based on the dimensions of the test specimen. Tabs were manufactured out of aluminum. Dimensions used can be seen in Figure 5-5.

The tabs were bonded to the kevlar specimen using a two-part industrial strength epoxy. After mixing M-Bond type 10 curing agent into M-Bond adhesive resin (Type AE), the epoxy was placed between the tabs and the specimen. The specimen was then clamped in a vice and allowed to set overnight.

Test Procedure: The use of ASTM 3039 test method works well for orthotropic specimens. This is due to the uniform state of stress that is produced as tensile loading is induced [10]. The testing on the kevlar was to obtain tensile material properties in both the transverse and longitudinal directions. The test procedure was conducted like that used for the steel specimens.

The cross-head speed to be used is also specified in ASTM 3039/3039M and, like the tensile testing of the steel, is given in terms of strain rate. In this case, the recommended speed should be such that failure is produced in 1 to 10 minutes. The ASTM further recommends that if failure points are unknown, a standard head displacement rate of 0.05 in/min is recommended. A speed of 0.1 in/min was found to produce failure within the limits specified above (normally between 5 and 7 minutes).

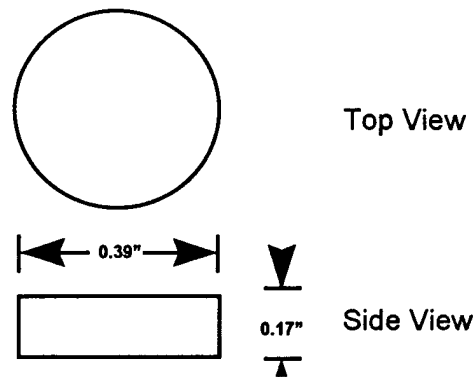


Figure 5-1: Diagram of rubber specimen.

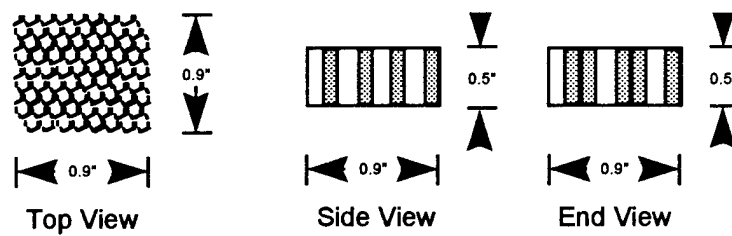


Figure 5-2: Diagram of honeycomb specimen.

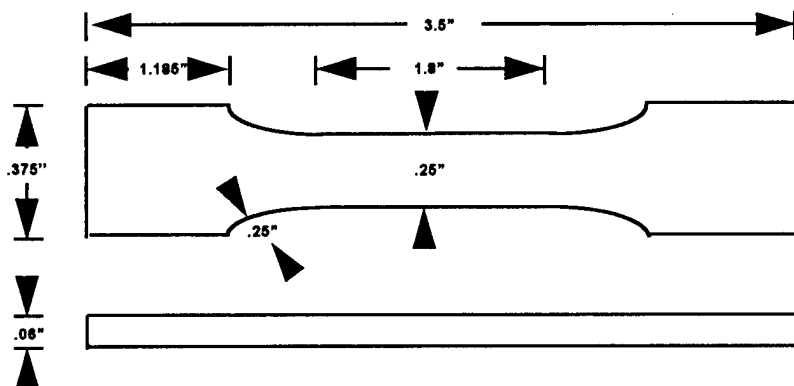
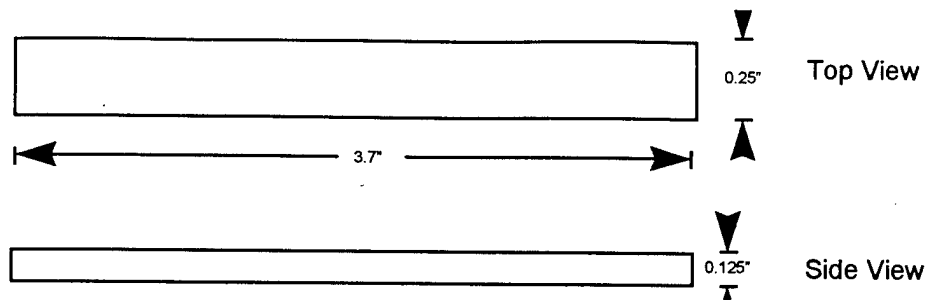
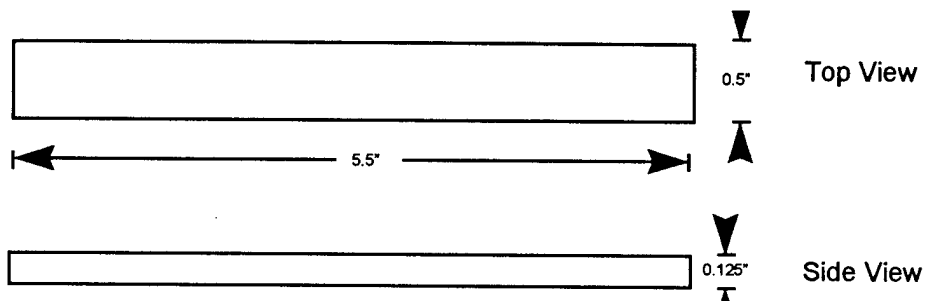


Figure 5-3: Diagram of steel specimen





a.) Transverse specimen.



b.) Longitudinal specimen.

Figure 5-4: Diagrams of kevlar specimen.

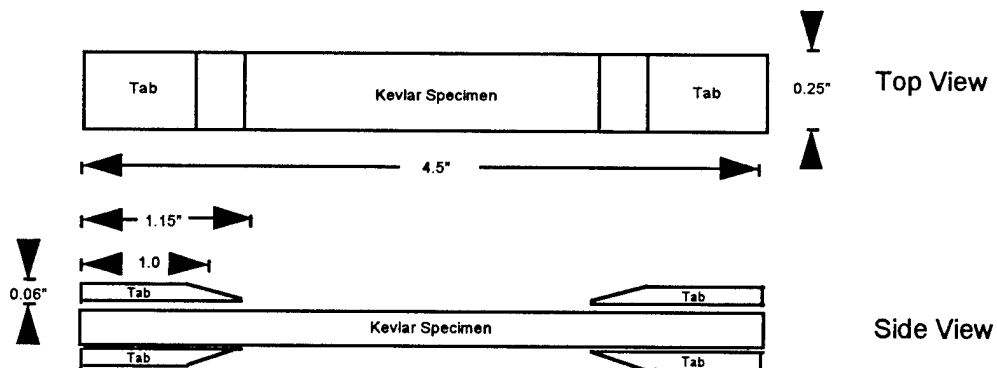


Figure 5-5: Diagram of tab dimensions.

## 6. TEST RESULTS

### 6.a. Rubber

The primary goal of the rubber compression testing was to obtain accurate data on the elasticity of the rubber used in the boots and compare this data for different boots. The stress vs strain plots for the rubber samples are enclosed as Appendix B.

As stated previously, the raw data from the Instron machine's computer was downloaded as an ASCII file of data points in the form of force (lbs) and displacement (in). In MATLAB, this data was converted to stress and strain. This data was then plotted to simplify comparison of the specimens. (See Appendix B.) It is clear that the rubber from the specimens of each boot behaved almost identically, regardless from which boot the specimen originated.

The initial linear region was linearized in MATLAB in order to most accurately calculate a Young's modulus of elasticity. The Young's moduli are listed in Table 6-1.

It is noteworthy that all of the Young's moduli, with the exception of the first sample of the first boot, are within 5% of the average. If the first boot's first sample was discarded, the average Young's modulus would be 1603.9 psi. The remaining five samples are all within 3.8% of this value.

In addition to having such close Young's moduli, all of the samples' elastic regions lasted until strain values were approximately 0.3 in/in.

### **6.b. Aluminum Honeycomb**

The most critical values to be obtained from the compressive tests of the honeycomb specimens was the failure strength of the honeycomb in the compressive/downward direction. That is, at what pressure the honeycomb will begin to collapse in the vertical direction. Plots of the stress vs strain curves are given in Appendix C. The results for failure in all three directions are given in Table 6-2. It is clear that the vertical strength of the honeycomb is far greater than the strength in either longitudinal or transverse directions.

As was done with the rubber specimens, the initial region was linearized utilizing MATLAB. These equations were then used to calculate Young's moduli for each sample in each direction. The results are given in Table 6-3. It is interesting to note that the values obtained from the overboot shank in the downward and longitudinal directions are considerably different than the other samples which are relatively close. This could be the result of weaker bonding between the sheets of aluminum that make up the honeycomb. Since the failure strength, not Young's modulus, was considered the most critical property and given the limited amount of sampling material, no effort was made to test additional samples to find out if other honeycomb samples would behave the same as the overboot sample.

### **6.c. Stainless Steel**

The steel testing was unlike the two previous tests because not only was it a tensile test but some information about the

steel was known prior to the test as a result of the EDX discussed above. Additionally, one test specimen came from one boot (Boot #1) while the other two samples came from a second boot (Boot #2). The values found for the three tensile tests are listed in Table 6-4.

Given the purpose of the blast boots, the critical properties can be considered the yield strength and the ultimate strength. Due to the EDX finding that the steel for both the shank upper and base was Type 302 stainless steel, the values in Table 6-4 can be compared to any number of references. Depending on the amount of cold-working imposed on the steel during manufacturing, the values for .2% yield strength are within accepted values ranging from 30,000 psi [11] to 75,000 [12] psi if it has been cold-worked. This is also true for the values of ultimate strength. Expected values ranged from 90,000 psi [11] to 110,000 psi [13]. Clearly, the test values obtained for these properties are very accurate.

References indicated that modulus of elasticity should be approximately  $28 \times 10^6$  psi [14]. A plot of the elastic region of the stress vs strain curves for the three specimens is given in Appendix D. It can be seen that Young's modulus for Sample 1 (Boot #1) is lower than that of the other two specimens. It is important to mention that of all the data obtained, there will be more error associated with obtaining an accurate Young's modulus than any other. This is primarily due to possible slippage in the extensometer and inherent error in using a screw-type machine to accurate data early in a test.

#### 6.d. Kevlar

The tensile testing results for the kevlar specimens are given in Table 6-5. Stress vs strain curves for the specimens are given in Appendix E. As noted in Table 6-5, the first transverse specimen's tabs failed at some point during the testing. In fact, three of the four tabs failed. More accurately, the epoxy between the tabs and the specimen disbonded. This may have caused some degree of slippage at the point when disbonding occurred. Without knowing the point at which this happened, the resulting data was regarded as unreliable. Data is included in Table 6-5 only for comparison.

As a result of the failure of the tabbing process and given the limited number of samples, it was decided that tabs would not be used for the following specimen. This was based on earlier, preliminary testing to determine the appropriate crosshead speed that resulted in the failure of that specimen within the test region without the use of tabs. The second specimen failed in the test region as desired so it was decided to not use on the final specimen. As seen in Table 6-5, the second and third transverse specimen test results are extremely close.

As a result of lessons learned on the use of tabs in testing the transverse specimens, it was decided to not use tabs on any of the longitudinal test specimens. Unfortunately, the Instron machine's control panel experienced a software malfunction during the second test. The result was that the machine stopped recording displacement as the specimen was loaded. For this reason, no Young's modulus was obtainable. However, the load

applied to the specimen was recorded so failure stress was obtained and should be considered as accurate. Longitudinal test results are given in Table 6-6.

The failure stress for both transverse and longitudinal directions should be considered to be the same. This was expected since the layers of the kevlar are applied in a 0/90 manner. That is, each layer is applied perpendicular to the preceding layer.

Table 6-1. Test results of rubber testing.

Boot	Sample	Young's Modulus (psi)
1	1	1416.1
1	2	1544.5
1	3	1647.3
2	1	1623.0
2	2	1561.1
2	3	1643.7
	<b>Average</b>	<b>1572.6</b>

Table 6-2. Test results of honeycomb testing (failure strengths).

	Vertical (psi)	Longitudinal (psi)	Transverse (psi)
Overboot Shank	4649	148	244
Boot #1 Shank	4643	169	201
Boot #2 Shank	5196	181	219
<b>Average</b>	<b>4829</b>	<b>166</b>	<b>221</b>

Table 6-3. Test results of honeycomb testing (Young's Moduli).

	Downward Young's Modulus (psi)	Longitudinal Young's Modulus (psi)	Transverse Young's Modulus (psi)
Overboot	95,500	13,290	3908
Boot #1	164,900	6616	4960
Boot #2	127,450	6418	4950
<b>Average</b>	<b>129,283</b>	<b>8775</b>	<b>4606</b>

Table 6-4. Test results of steel testing.

	0.2% Yield Strength (psi)	Ultimate Strength (psi)	Young's Modulus (psi)
Boot #1	36,710	95,818	26,300
Boot #2, Sample #1	39,370	99,070	29,700
Boot #2, Sample #2	40,040	99,270	31,200
<b>Average</b>	<b>38,707</b>	<b>98,052</b>	<b>29,066</b>



Table 6-5. Test results of transverse kevlar tests.

	Maximum Stress (psi)	Young's Modulus (psi)
Specimen #1	42,378*	239,560*
Specimen #2	44,884	106,320
Specimen #3	45,717	108,840
<b>Average</b>	<b>45,300**</b>	<b>107,580**</b>

\* Tabs failed.

\*\* Includes data from specimens 2 and 3 only.

Table 6-6. Test results of longitudinal kevlar tests.

	Maximum Stress (psi)	Young's Modulus (psi)
Specimen #1	45,412	374,850
Specimen #2	42,633	*
Specimen #3	39,788	255,770
<b>Average</b>	<b>42,611</b>	<b>315,310**</b>

\* Instron machine malfunctioned.

\*\* Includes data from specimens 1 and 3 only.

## 7. FINITE ELEMENT MODEL

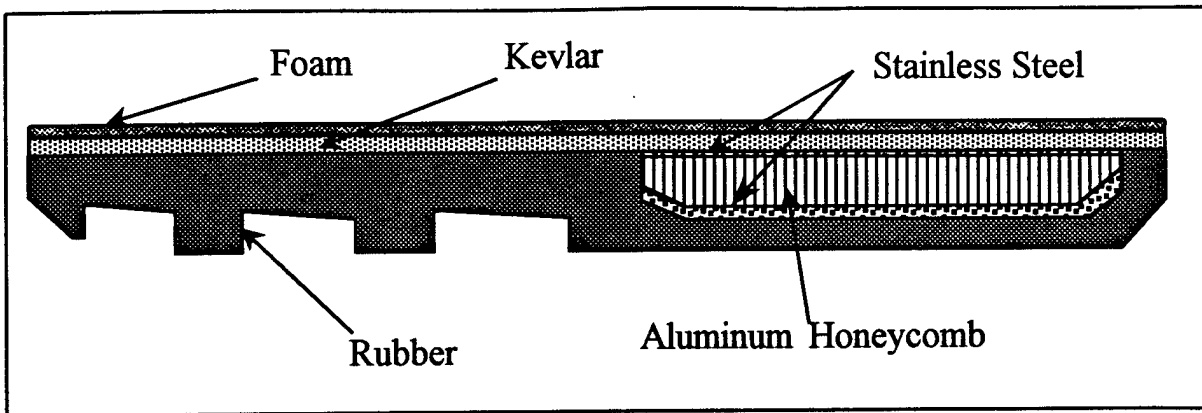
A preliminary Finite Element Model (FEM) has been developed to analyze the complex interactions characterized by a Anti-Personnel Mine (AP Mine) explosion triggered by a soldier stepping on a pressure switch actuator. The model was built utilizing the windows driven PATRAN Preprocessor. This program allows for easy manipulations of complex geometries. Once the mesh was generated, it was exported to the DYNA 3D, version 9.36. The FEM program simulates static as well as dynamic conditions and models the behavior of the materials subjected to various loads. Figure 7-1 shows the longitudinal and transverse cross-sections of the Anti-Mine boot. The model was simplified focusing on the a 3 in x 3 in cross section centered on the heel and ankle as seen in Figure 7-2 showing the FEM mesh including the individual components of the Anti-Mine boots. The boot shape has been modified to discount the rubber stabilizers along the outside edges of the sole. The blast wave in this case can be considered normal to the boot surface and exerting a force axially along the boot and the bone. A blast detonated off of this axis will have components perpendicular to the longitudinal axis of the bone creating bending moments. Material properties used in this simulation are the result of static testing conducted for this project. Dynamic loading such as that experienced from an explosion will result in higher values for some properties. For properties that were unavailable from testing, nominal values from compiled tables were selected [17].

Time of detonation of the mine is taken as the initial or zero time. At this time the model is subjected to a pressure wave consistent with those generated by a typical AP Mine. The US made M-14 mine was selected as the standard due to its similarity to a large group of mines produced throughout the world. It also allows for comparison to previous studies conducted [15]. In this preliminary model, the pressure wave is represented by a normally incident wave with a duration of 0.0175 ms and a peak pressure of 1941 psi. A load curve has been defined to describe the pressure as a function of time using Equations 7.1 and 7.2 [3].

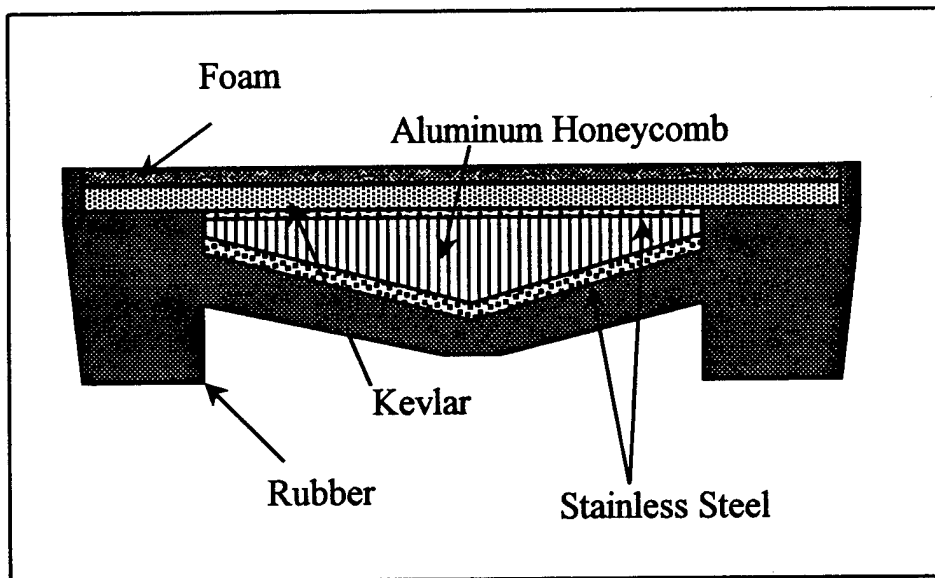
$$\frac{p_o}{p} = \frac{808 * \left[ 1 + \left( \frac{Z}{4.5} \right)^2 \right]}{\sqrt{1 + \left( \frac{Z}{0.048} \right)^2} * \sqrt{1 + \left( \frac{Z}{0.32} \right)^2} * \sqrt{1 + \left( \frac{Z}{1.35} \right)^2}} \quad \text{Eqn 7.1}$$

where

$$p = p_o * \left( 1 - \frac{t}{t_d} \right) * e^{-a * \left( \frac{t}{t_d} \right)} \quad \text{Eqn 7.2}$$



a. Transverse cross-section



b. Longitudinal cross-section.

Figure 7-1: Transverse and longitudinal cross-sections of the countermine boot.

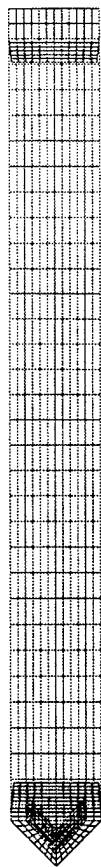


Figure 7-2a: Entire finite element model.

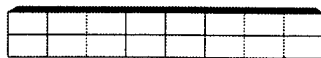


Figure 7-2b: Finite element model of kevlar liner.

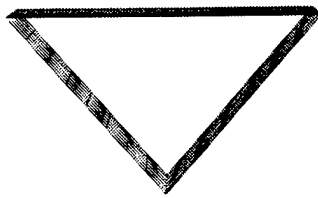


Figure 7-2c: Finite element model of stainless steel.

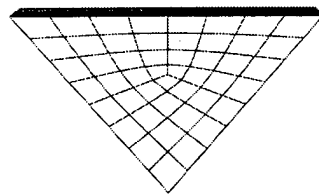


Figure 7-2d: Finite element model of aluminum honeycomb.

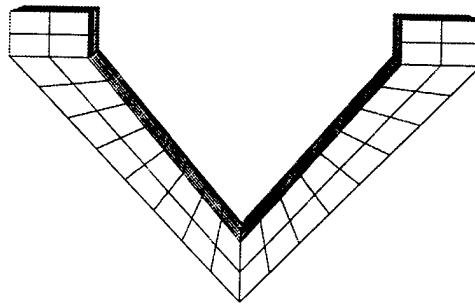


Figure 7-2e: Finite element model of rubber sole.

## 8. BLAST EFFECTS ON COUNTERMINE BOOTS

The blast wave is represented by pressure waves incident normal to the surface of the sole of the boot. The pressure wave traveled through the boot and into the lower extremities. As it transversed the different parts of the boot, it established a varying stress field as seen in Figure 8-1.

The rubber which was directly exposed to the incident wave experienced localized failure along the surface by 2.6 ms. This failure took the form of rubber particles separating from the sole and being forced upwards by the pressure wave. There is an associated energy loss in the system with the loss of particles that is not accounted for in the model. Figure 8-2 shows the stress field variation with time for several elements along the surface of the rubber sole. (The locations of the elements are given in Appendix F.) The rubber has undergone a gross deformation exceeding the compressive strength of the rubber as determined in the material testing for this project. This means the rubber has lost its capacity to absorb any additional energy from the explosion.

At the final state of 4 ms, it can be readily seen that the other materials of the boot have also suffered various degrees of deformation. The thin shells representing the Type 302 Stainless Steel are treated as elastic-plastic materials. In Figure 8-3, representative elements along the sides steel is compressed and yields within the first 0.4 ms. It continues to contribute to



the strength of the boot until approximately 1.6 ms at which time the failure strength is reached. The top of the steel shell, shown in Figure 8-4, also yields quickly but some sections continue to provide strength until 2.2 ms.

The honeycomb is compacted as the blast wave is transmitted upwards. As the cells of the honeycomb collapse they absorb the energy of the blast. Figure 8-5 shows representative elements in each section of the honeycomb. The material began to compact after 0.2 ms. Compaction continued until between 1.0 and 1.3 ms. At this time there is a sudden increase in stress as the honeycomb is fully compacted and reverts to the strength of a solid aluminum bar of the same dimensions.

The Kevlar layer is designed to prevent fragments from penetrating the insole of the boot and impacting on the foot and leg. This preliminary model which does not account for fragments cannot speak to its effectiveness at stopping fragments. However, the material is subjected to large stress fields and does undergo some permanent deformation which may indicate a possible path for fragments to penetrate. In particular the stress toward the center of the section exceed the failure strength as shown in Figure 8-6. The strength of the kevlar does provide limited energy absorption during its deformation.

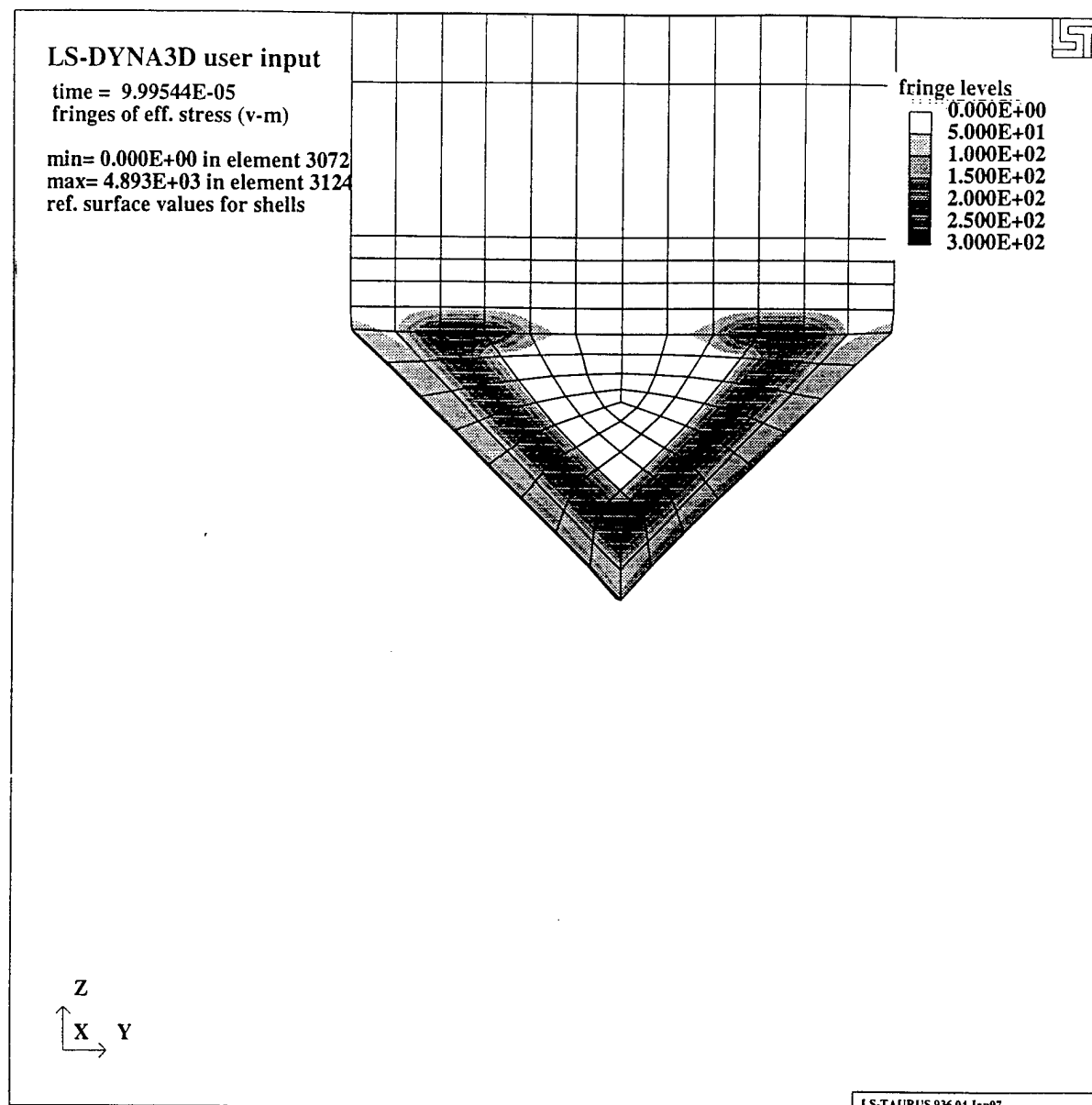


Figure 8-1a: Von Mises Effective Stress Fields at  $9.9954 \times 10^{-5}$  seconds in the Anti-Mine boot. As the blast wave progresses through the boot the varying stress fields are visible centering around the steel shell.

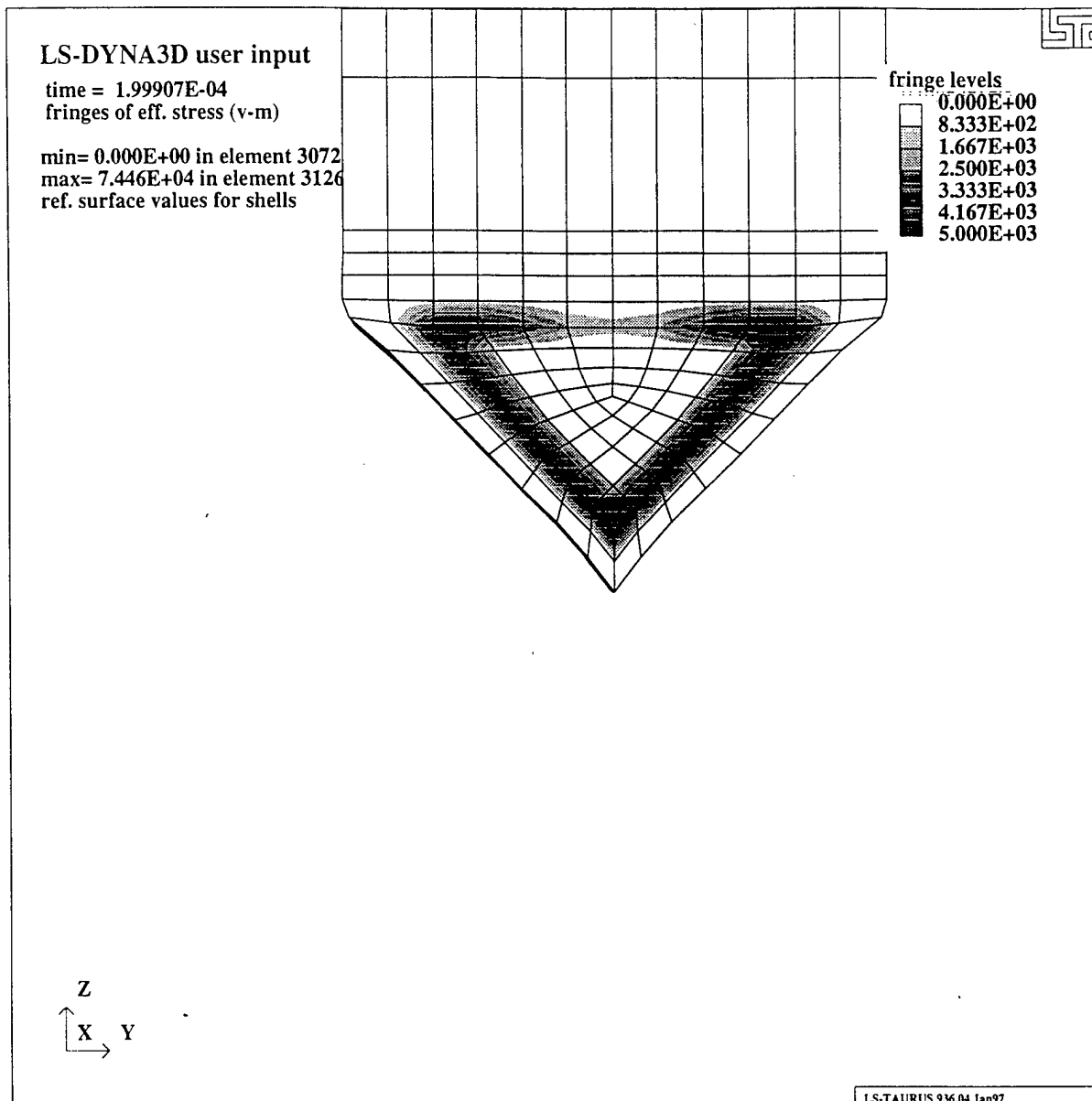


Figure 8-1b: Von Mises Effective Stress Fields at  $1.9991 \times 10^{-4}$  seconds in the Anti-Mine boot. As the blast wave progresses through the boot the varying stress fields are visible centering around the steel shell.

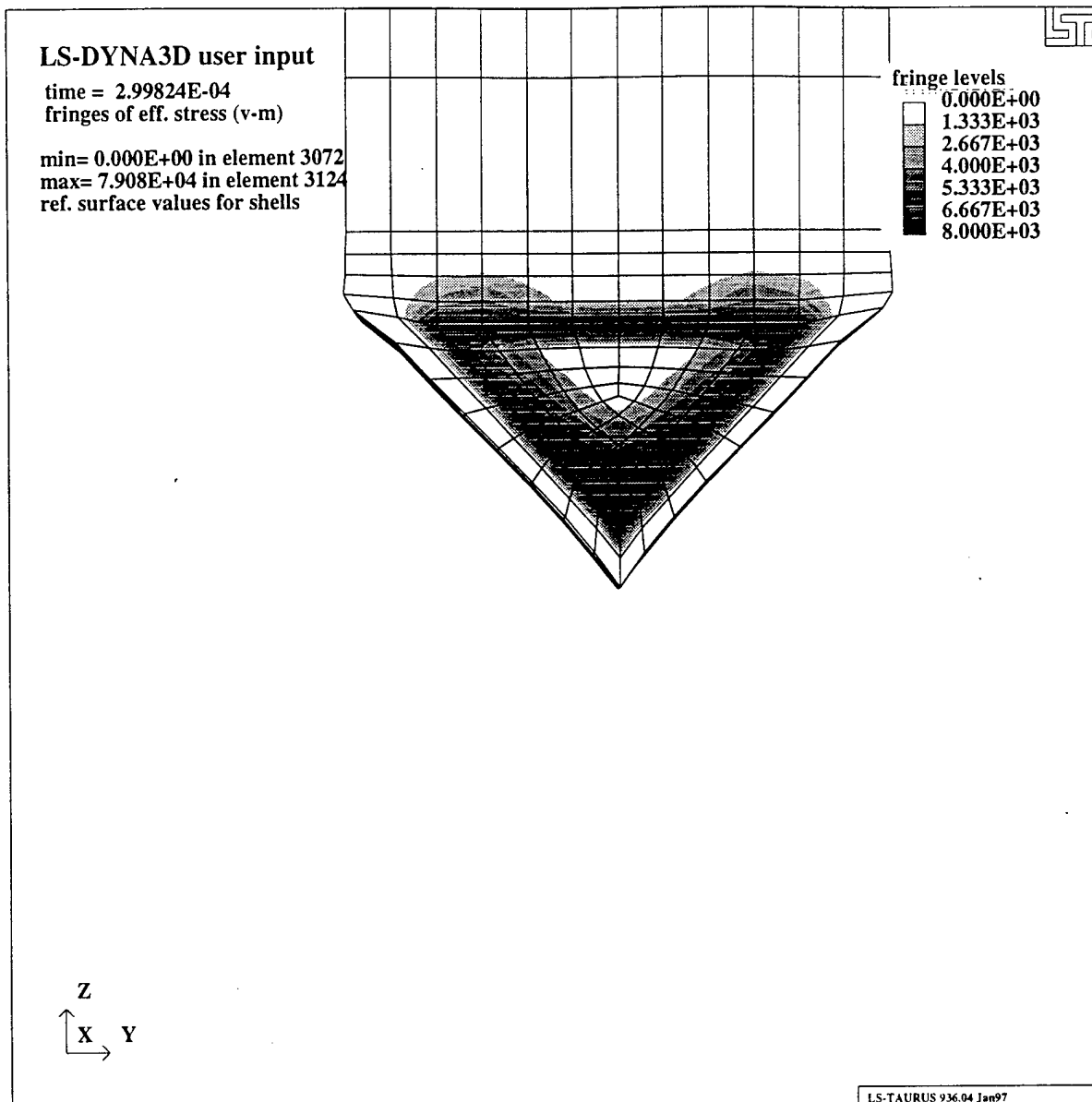


Figure 8-1c: Von Mises Effective Stress Fields at  $2.9982 \times 10^{-4}$  seconds in the Anti-Mine boot. As the blast wave progresses through the boot the varying stress fields are visible centering around the steel shell.

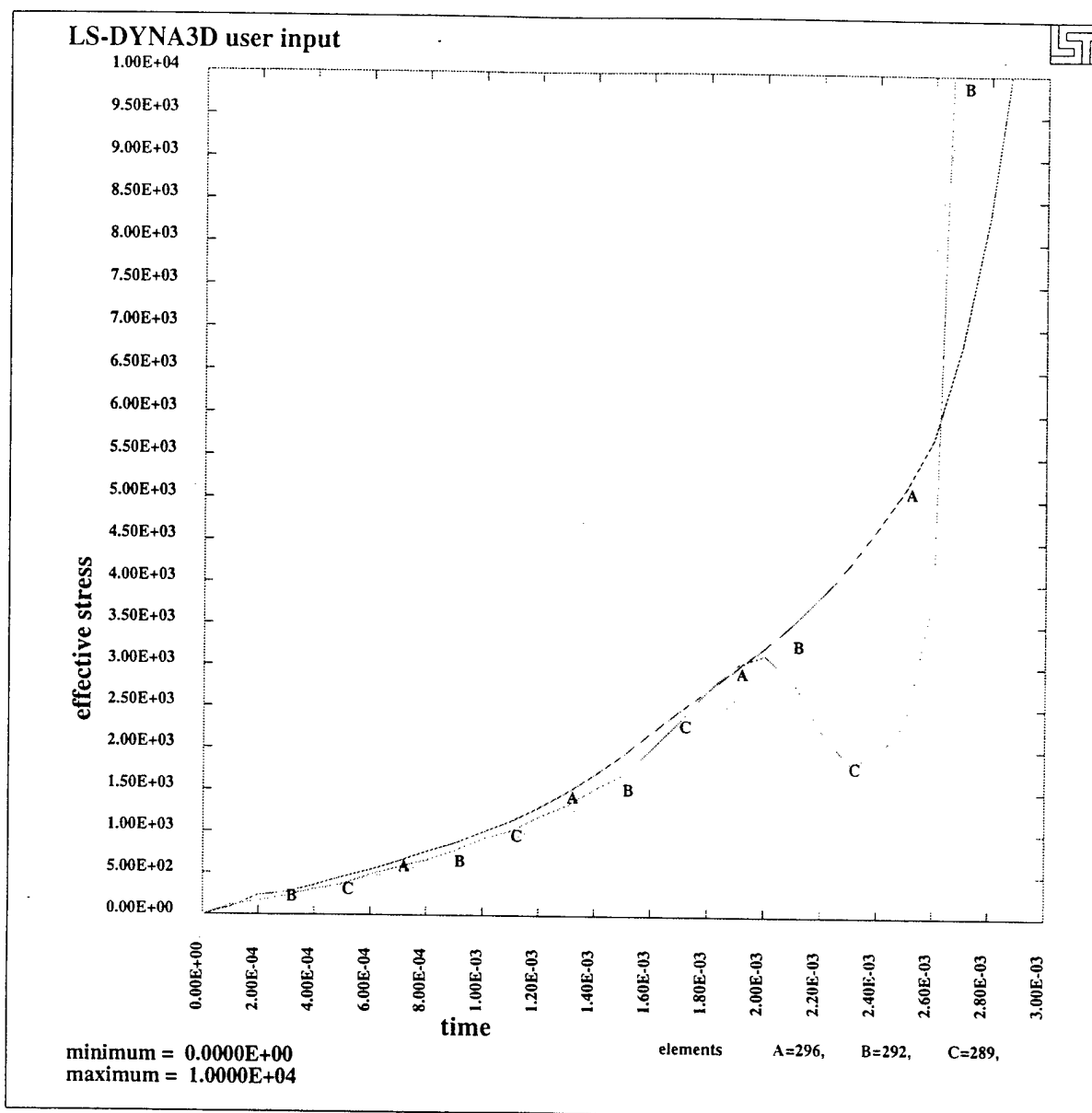


Figure 8-2: Von Mises Effective Stress representing elements along the surface of the rubber sole. Note the sudden increase in slope between 2.4 and 2.6 ms as the rubber fails at a stress of 8000 psi.

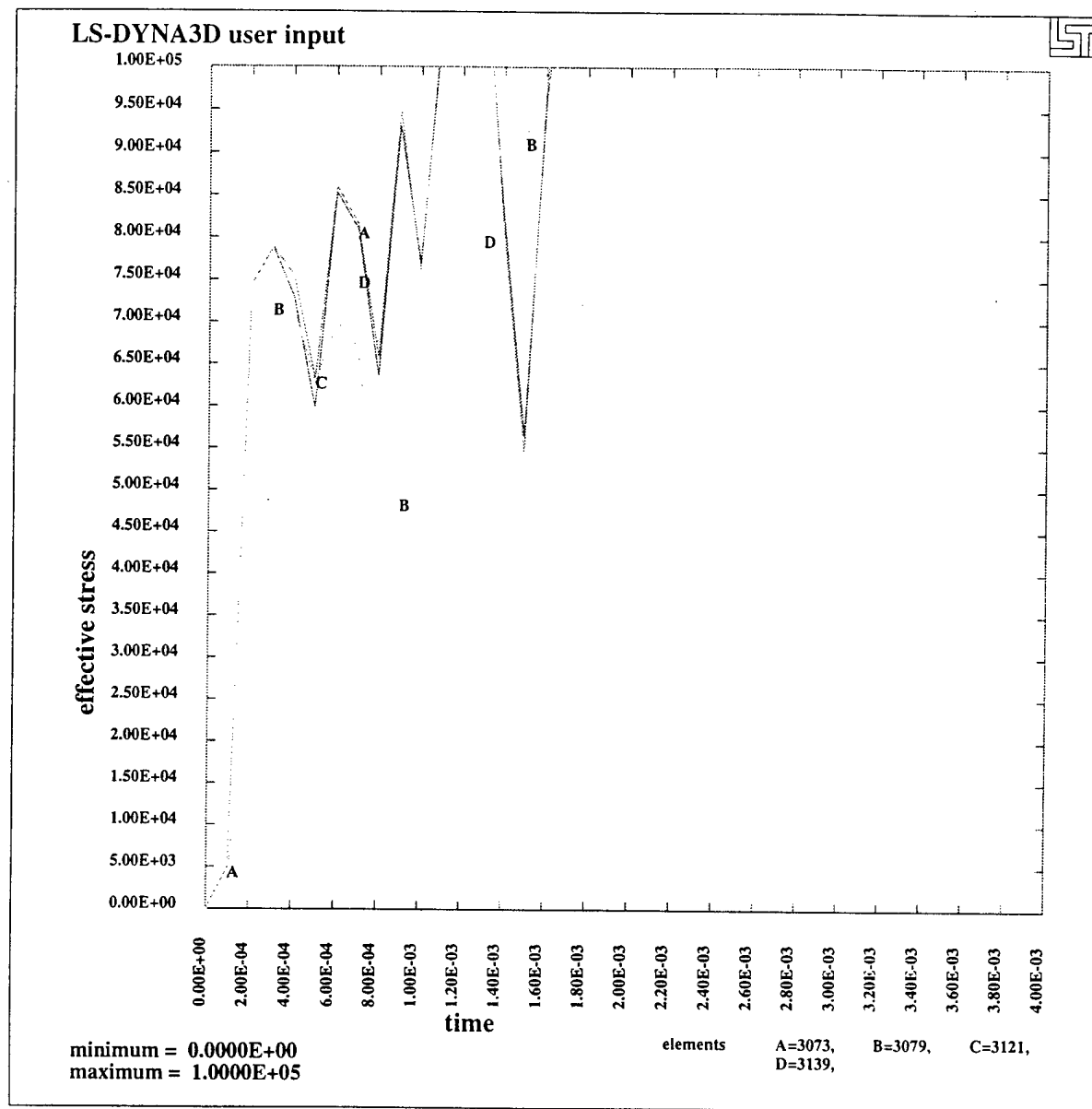


Figure 8-3: Von Mises Effective Stress for representative elements along the sides of the steel shell. Note failure strength is reached for all elements by 1.6 ms.

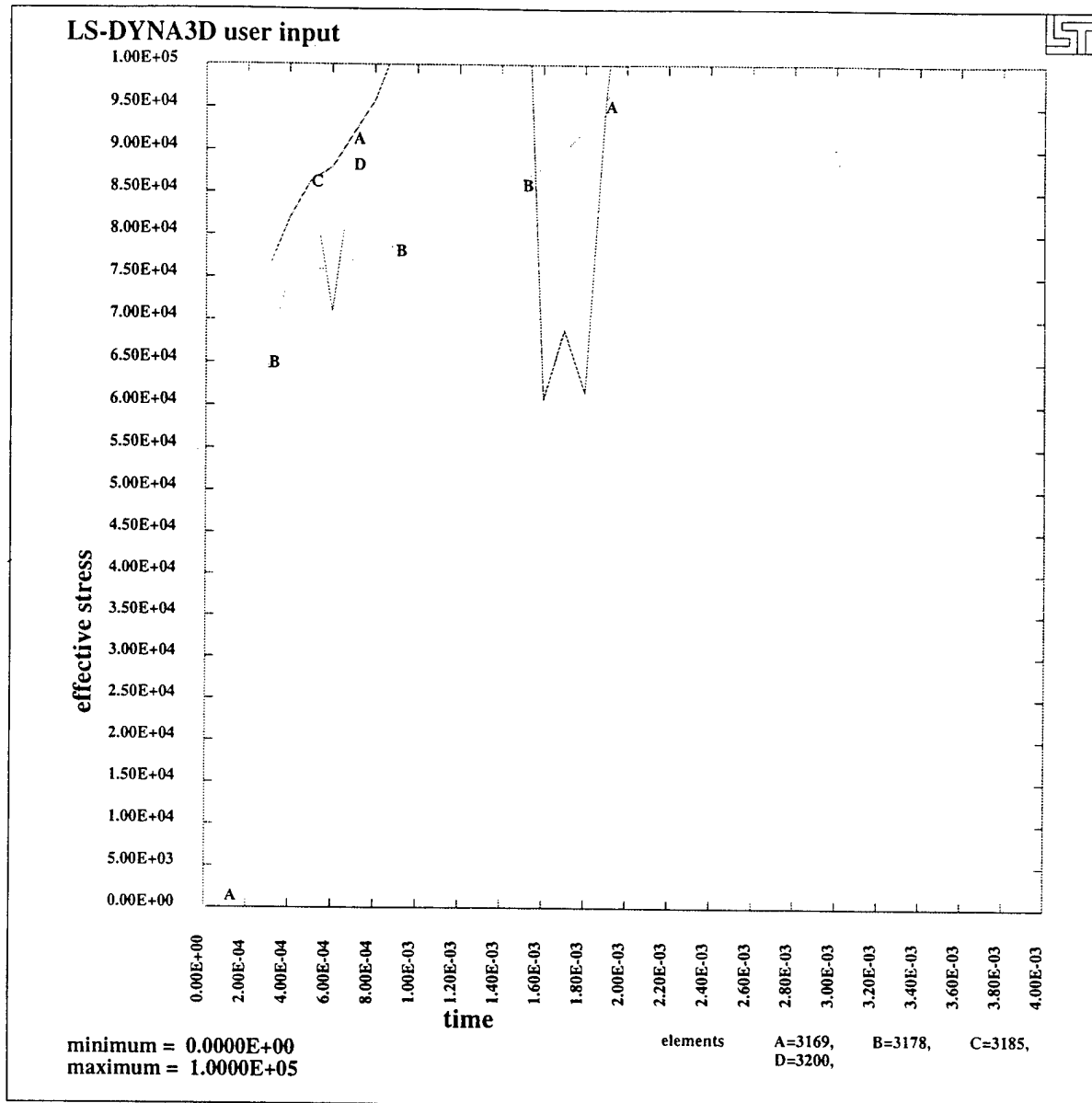


Figure 8-4: Von Mises Effective Stress for representative elements along the top of the steel shell. Note failure strength is reached for all elements by 2.2 ms.

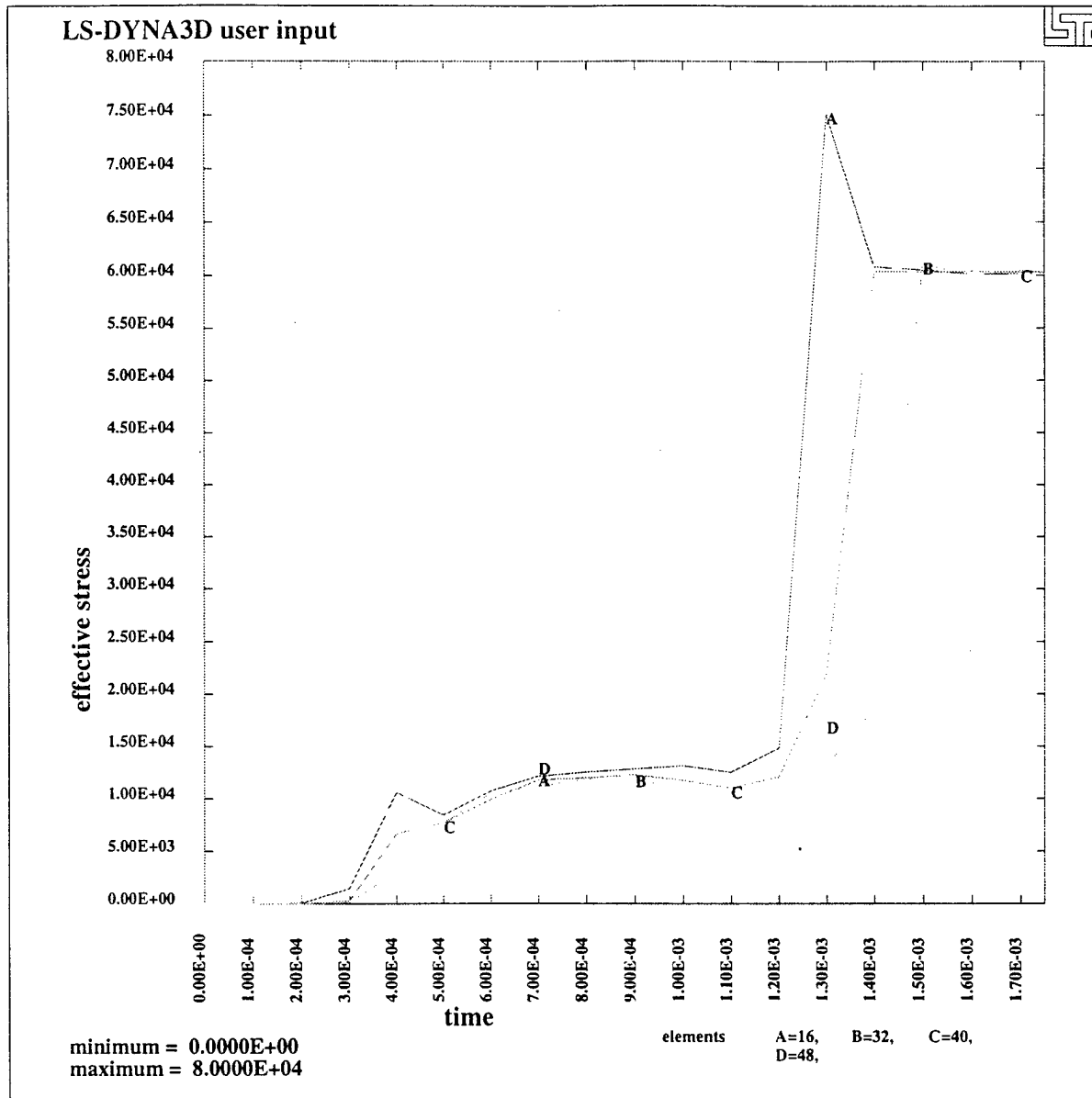


Figure 8-5: Von Mises Effective Stress for representative elements of the Aluminum Honeycomb. Note the compaction of the honeycomb between 0.2 and 1.3 ms. At the time the honeycomb is fully compacted.



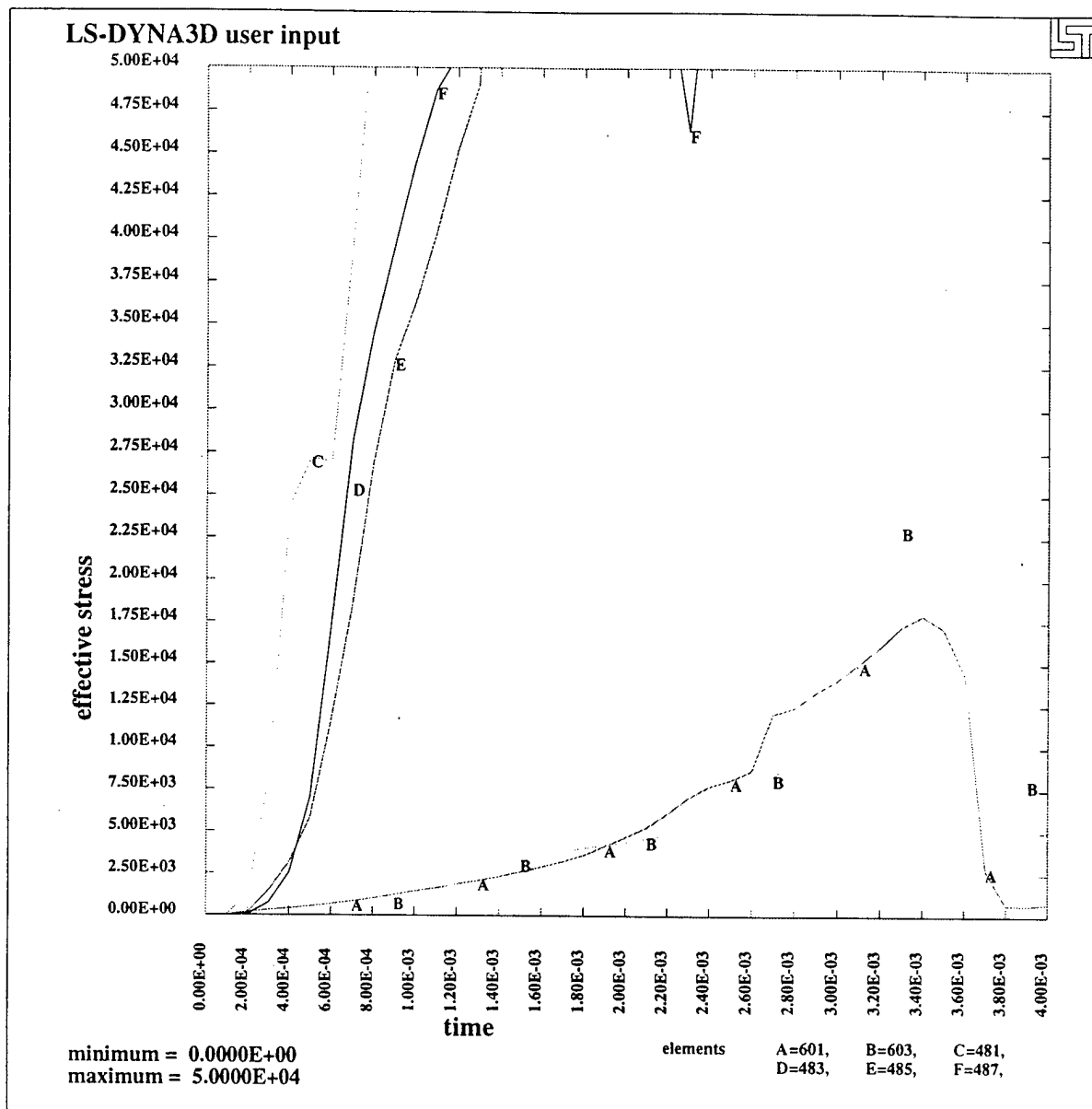


Figure 8-6: Representative elements along the surface of the Kevlar layer. The curves proceed from the outer edge (A) to the center (F). Note the inside elements all fail within 1.4 ms.

## 9. BLAST EFFECTS ON THE LOWER EXTREMITIES

This model attempts to represent the mechanical properties of the lower extremities by a skeletal frame of bone only. Follow on models will have to include the soft tissue to give a more accurate view of the energy absorbing properties of the body. The mechanical properties of bones and other organic materials are varied and dependent on many different circumstances. The values used for this model are nominal values adopted from available literature to represent an average of properties [15, 16]. It seems appropriate to assume the users of these boots will be by and large healthy individuals between 18-25. The properties for healthy members of this age group tend to be greater than the average. Thus the values used should be considered conservative estimates.

There are several methods to classifying injuries to the lower extremities and the breaking of bones. For ease in understanding this report, descriptive names for the types of fractures are explained below [16]. A Simple Fracture is considered a simple break of the bone into 2 distinct parts. A Complex Fracture is a break into 3 or more pieces. A Comminuted Fracture has been described as a crushing fracture because it is characterized by the breaking of the bone into many small pieces. Fractures can also be described as Displaced or Undisplaced. An Undisplaced fracture means the bone has remained essentially in the same plane and is aligned normally. Alternatively, a Displaced fracture is out of alignment and is a much more serious injury.

Adult bones are essentially brittle materials becoming more brittle with age. Brittle materials load up linearly to some critical strength value and then fail. As we examine the next set of figures we will see a build up to some stress level greater than the failure strength of the bone. This signifies the breaking of the bone. These elements were constructed using elastic material model. This doesn't allow the material to fail as it normally would.

The pressure wave traveling through the feet exceeds the failure strength and quickly fails by 0.4 ms as seen in Figure 9-1. The wave enters the ankle and base of the tibia at approximately 0.3 ms and also fails within the first millisecond, Figure 9-2. This same figure also shows the shear stress for this region which also suggests a rapid failure.

Figure 9-3 shows the final progression of the pressure wave up the lower extremities. At 4 ms the wave has traveled approximately one quarter of the distance of the tibia. The damage to the tibia at 1/8 of the distance is characterized by Figure 9-4. This figure shows the wave begin to affect this area at 1.4 ms with failure occurring at 2.4 ms.

Finally, we look at an area a quarter distance from the bottom of the tibia. By 4.0 ms this region is just starting to feel the affects of the blast. Preliminary indications however show a much reduced stress level in Figure 9-5. This stress does not exceed the failure strength of the bone remains intact above this point.

Table 9-1: Properties of Human Bone used in FEM Model

Density	0.018
Young's Modulus	14,500 psi
Poisson's Ratio	.3
Failure Strength	725 psi

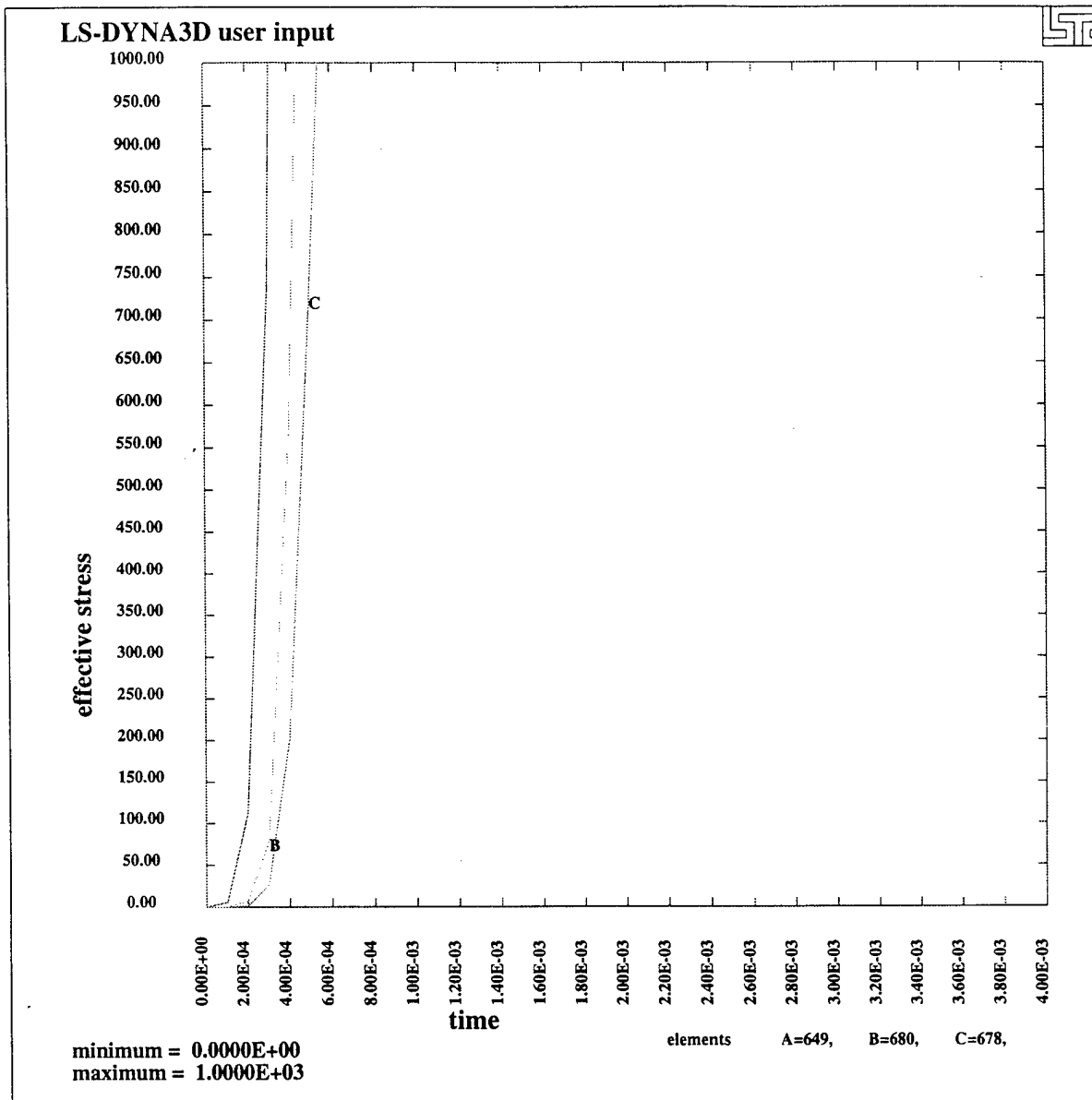


Figure 9-1: Von Mises Effective Stress for the foot region. These representative elements along the base of the foot show a rapid failure.

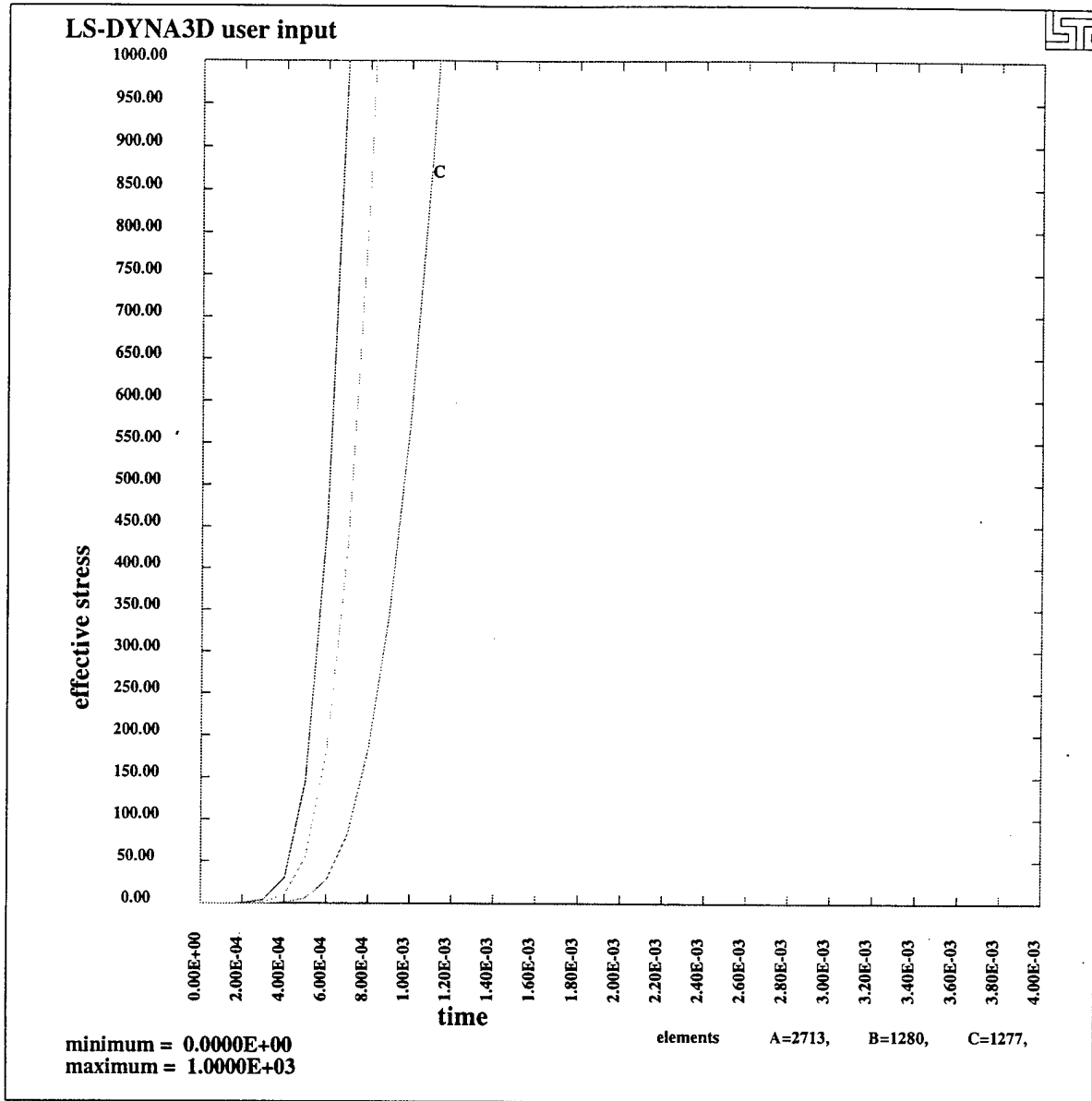


Figure 9-2a: Von Mises Effective Stress for the ankle region. These representative elements show a rapid failure within 1.0 ms.

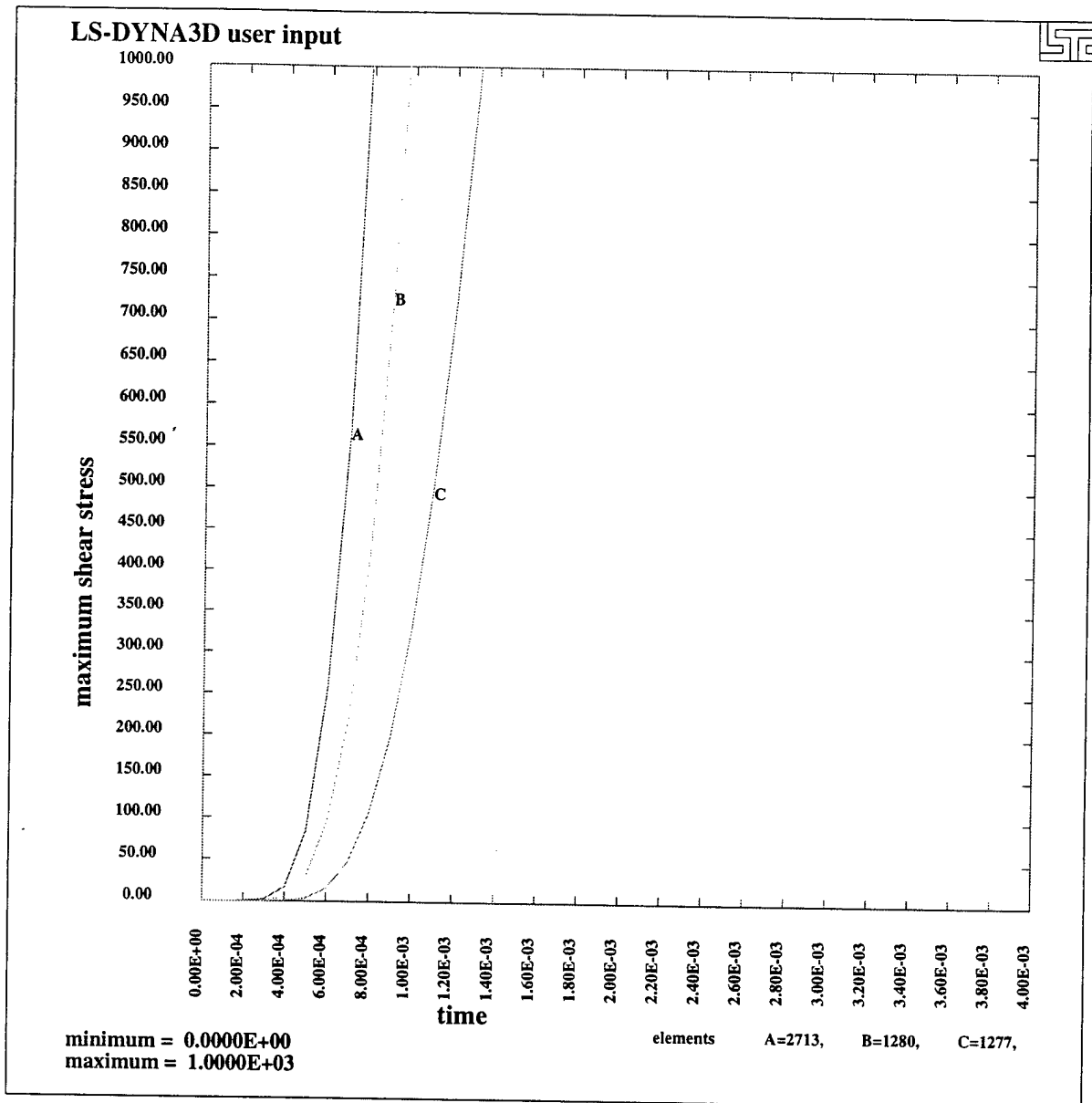


Figure 9-2b: Von Mises Maximum Shear Stress for the ankle region. These representative elements show a rapid failure within 1.0 ms.

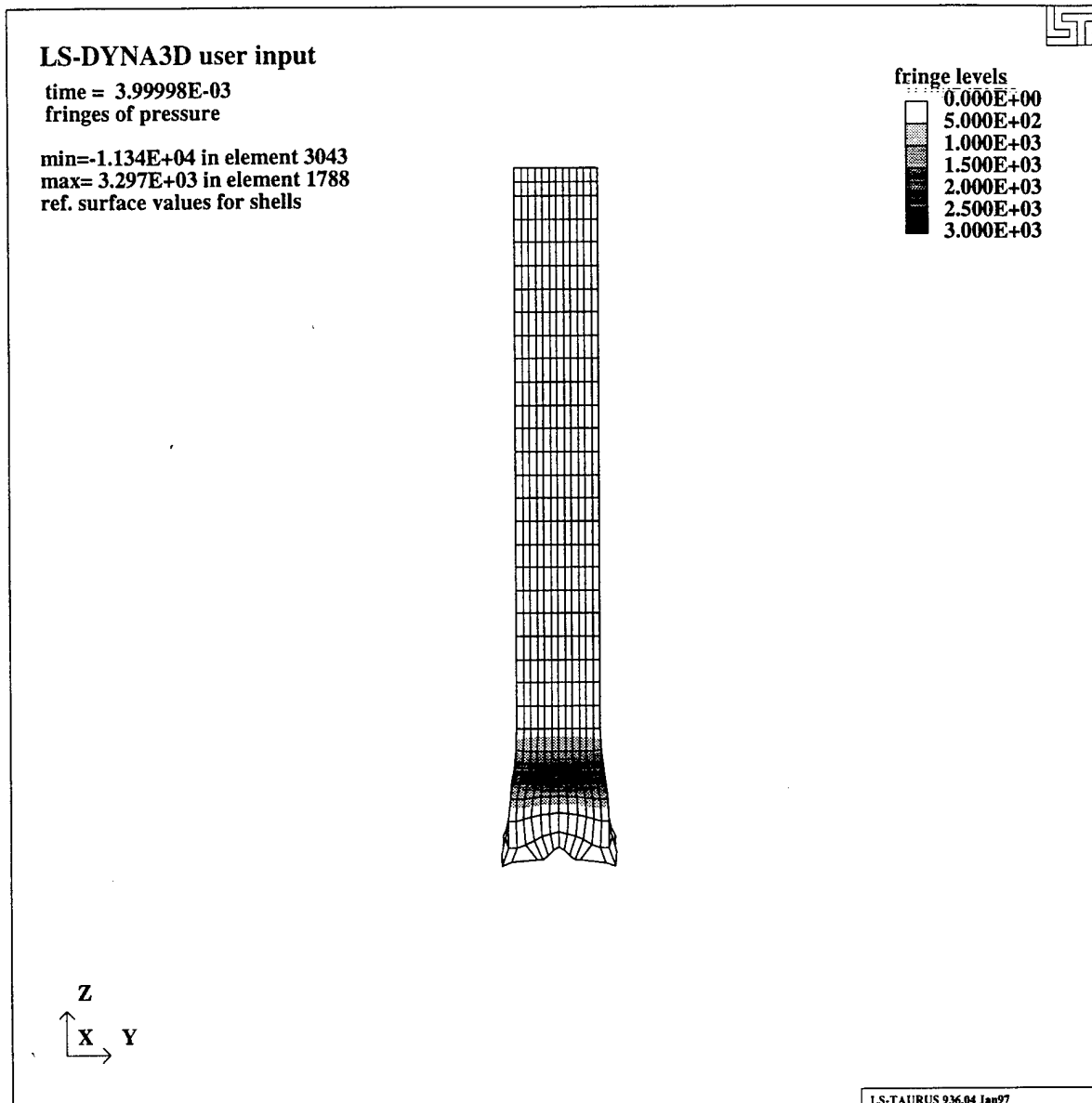


Figure 9-3: Progression of Pressure wave through the lower extremities at 4.0 ms



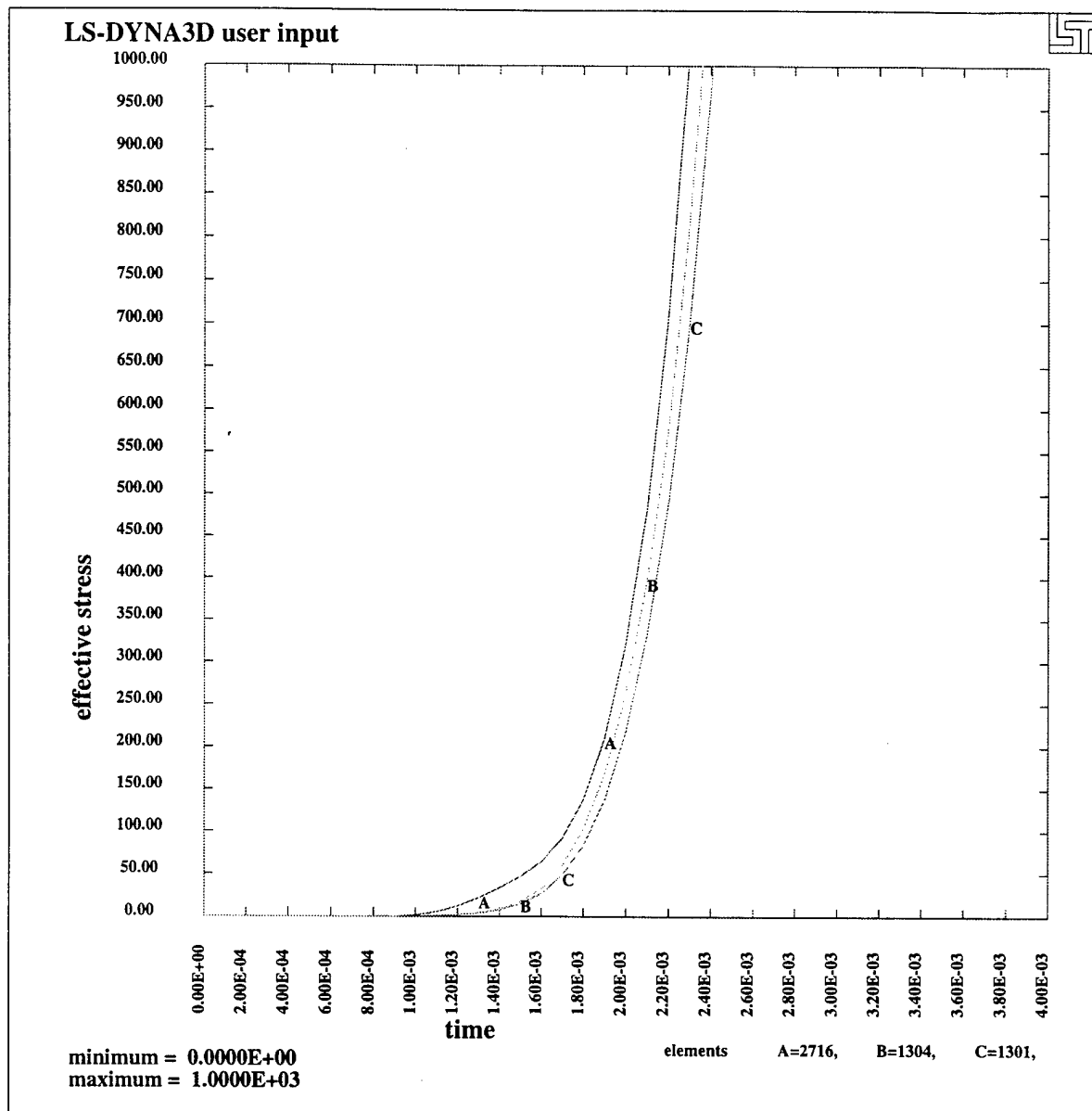


Figure 9-4a: Von Mises Effective Stress for representative elements 1/8 distance up the tibia. Note failure within 2.4 ms.

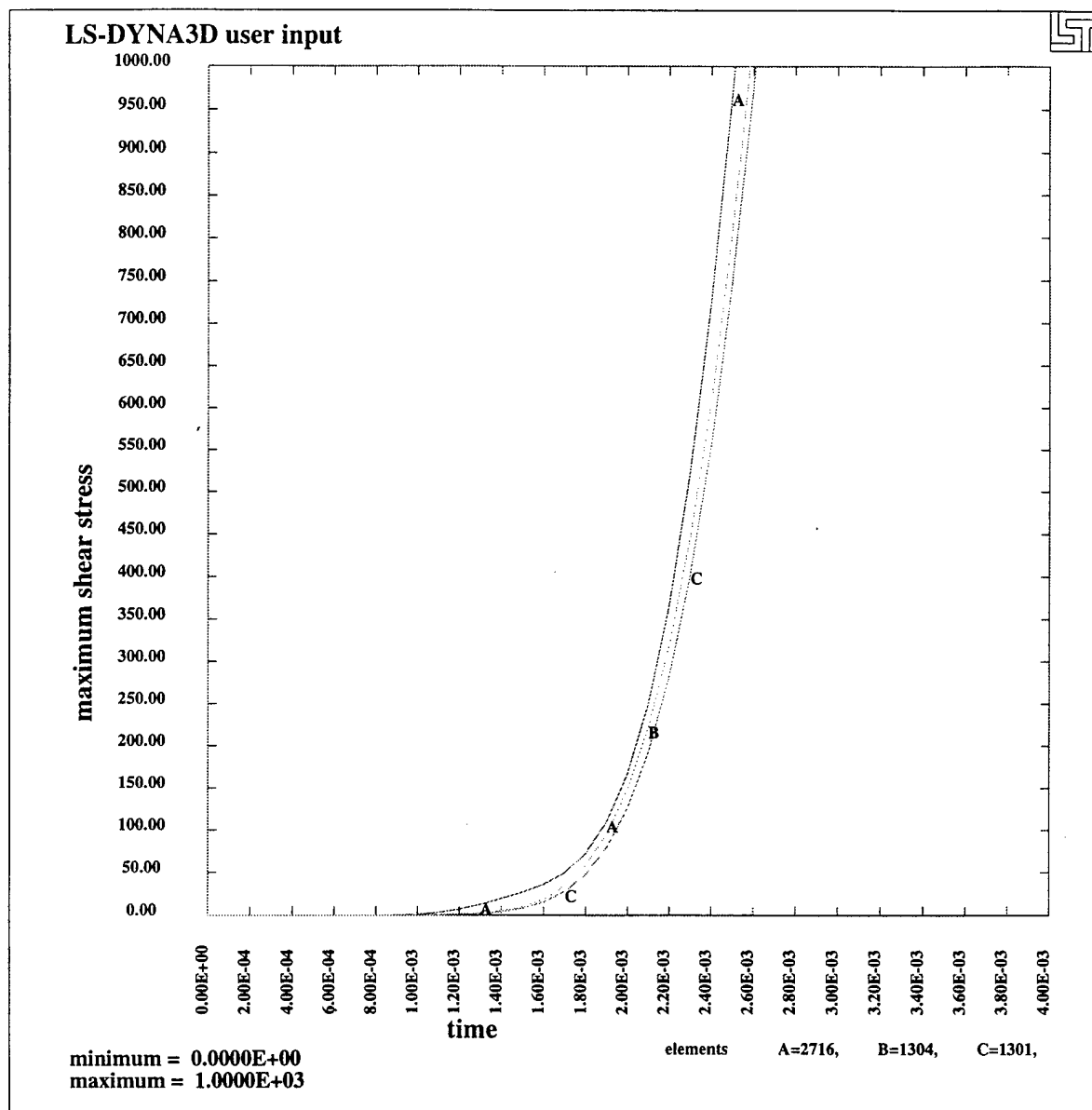


Figure 9-4b: Von Mises Maximum Shear Stress for representative elements 1/8 distance up the tibia. Note failure within 2.4 ms.

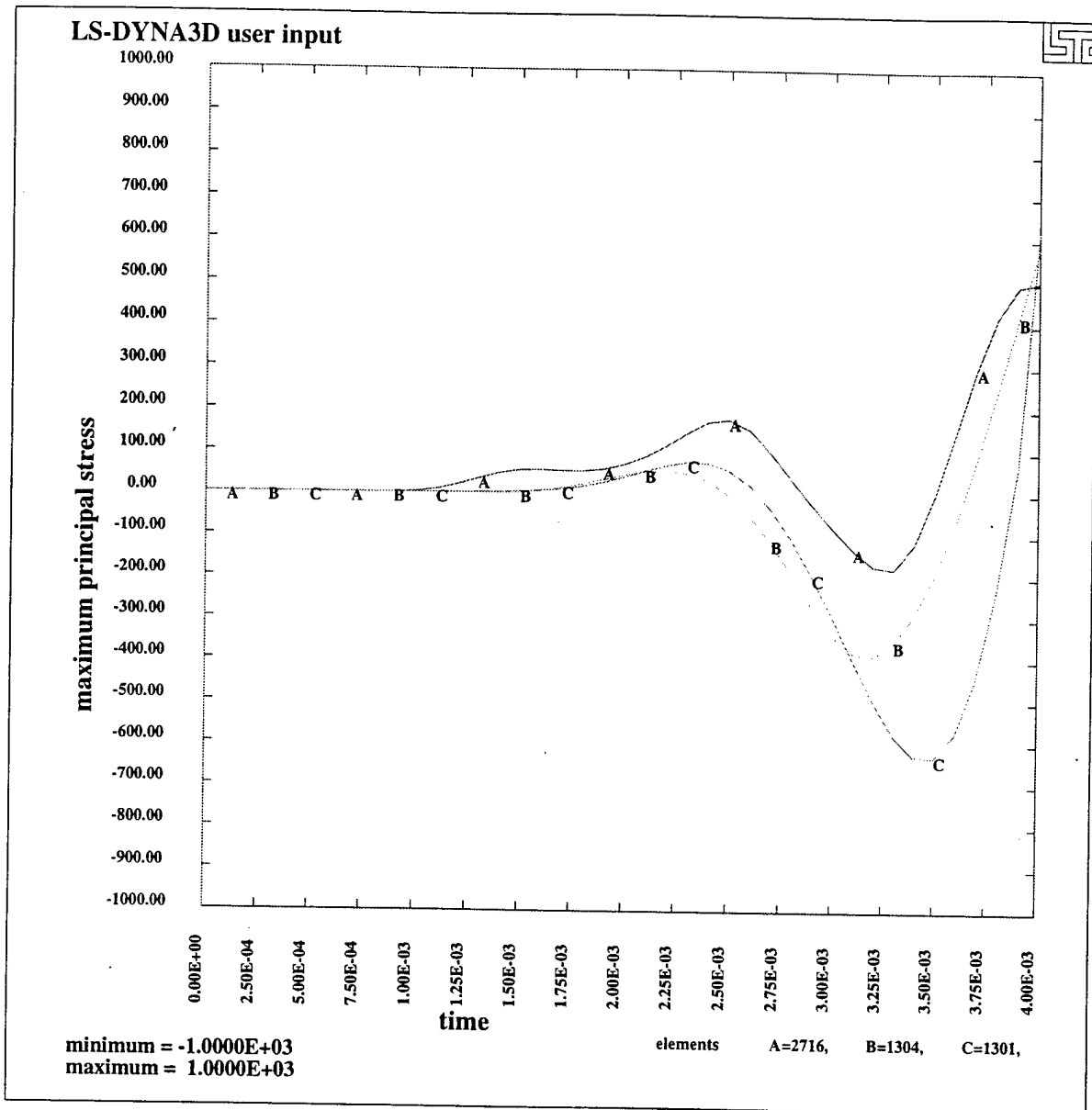


Figure 9-4c: Maximum Principal Stress for representative elements 1/8 distance up the tibia. Note failure within 2.4 ms.

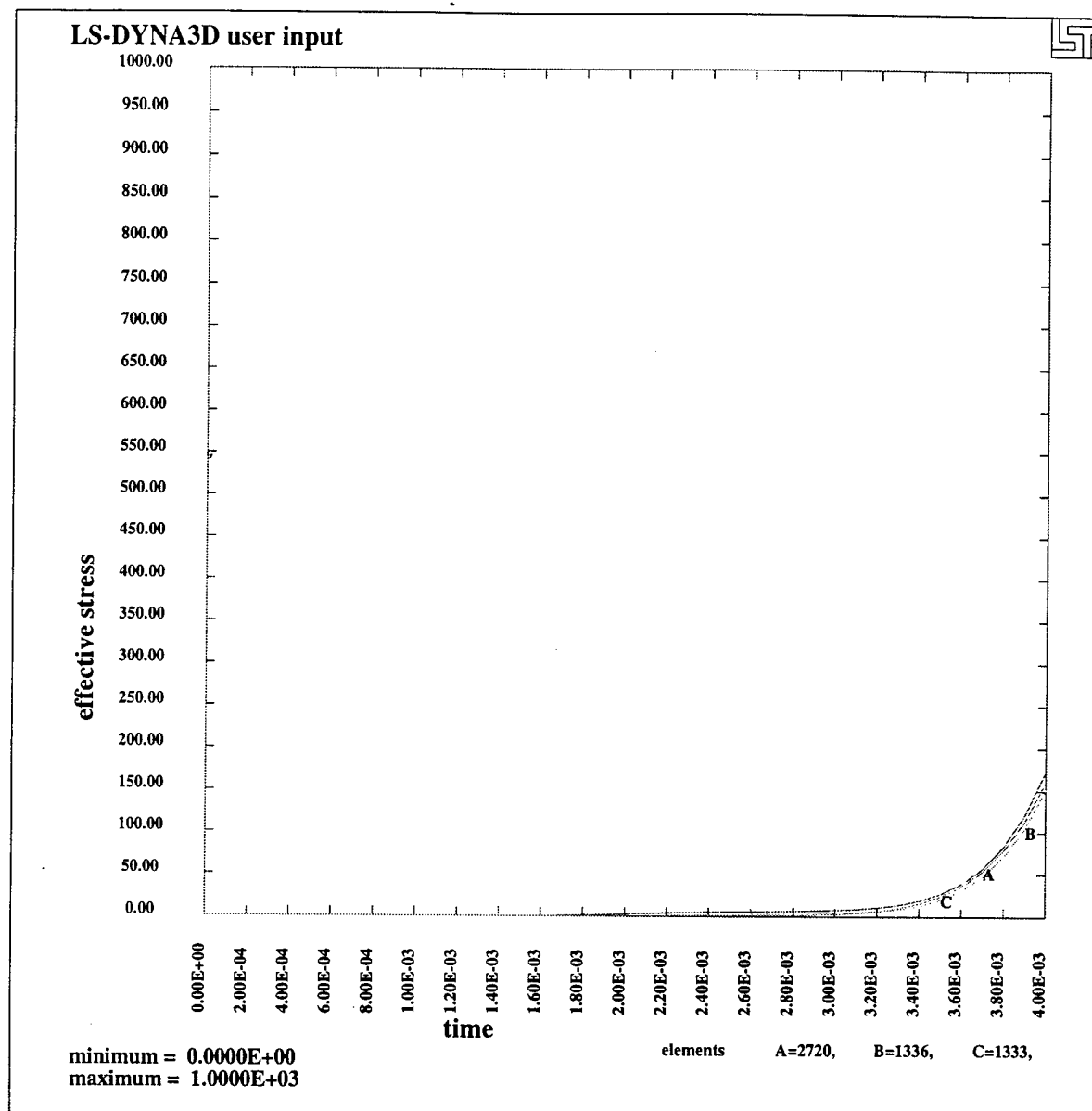


Figure 9-5a: Von Mises Effective Stress for representative elements  $\frac{1}{4}$  distance up the tibia. Note stress remains below failures.

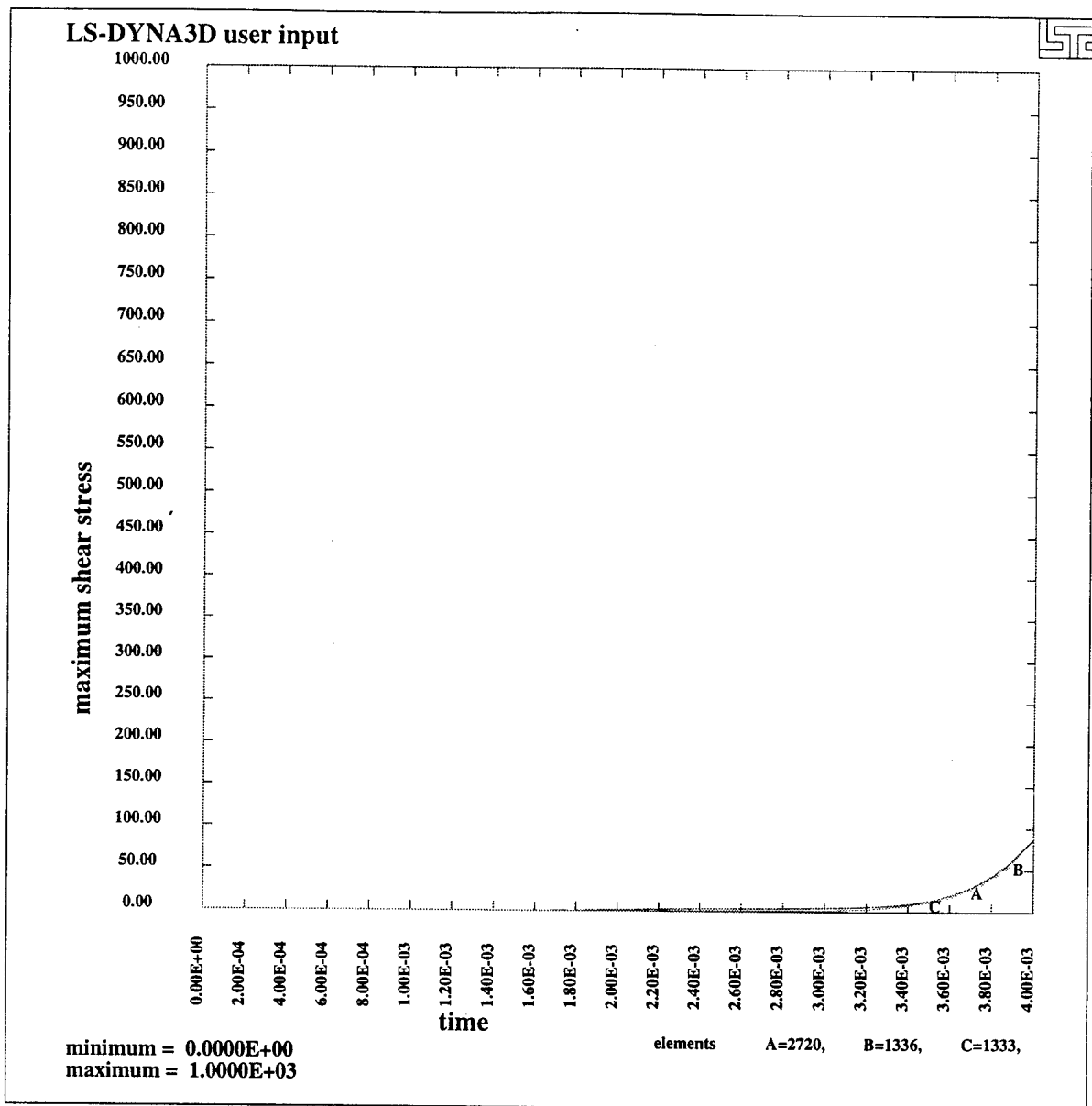


Figure 9-5b: Von Mises Maximum Shear Stress for representative elements  $\frac{1}{4}$  distance up the tibia. Note stress remains below failures.

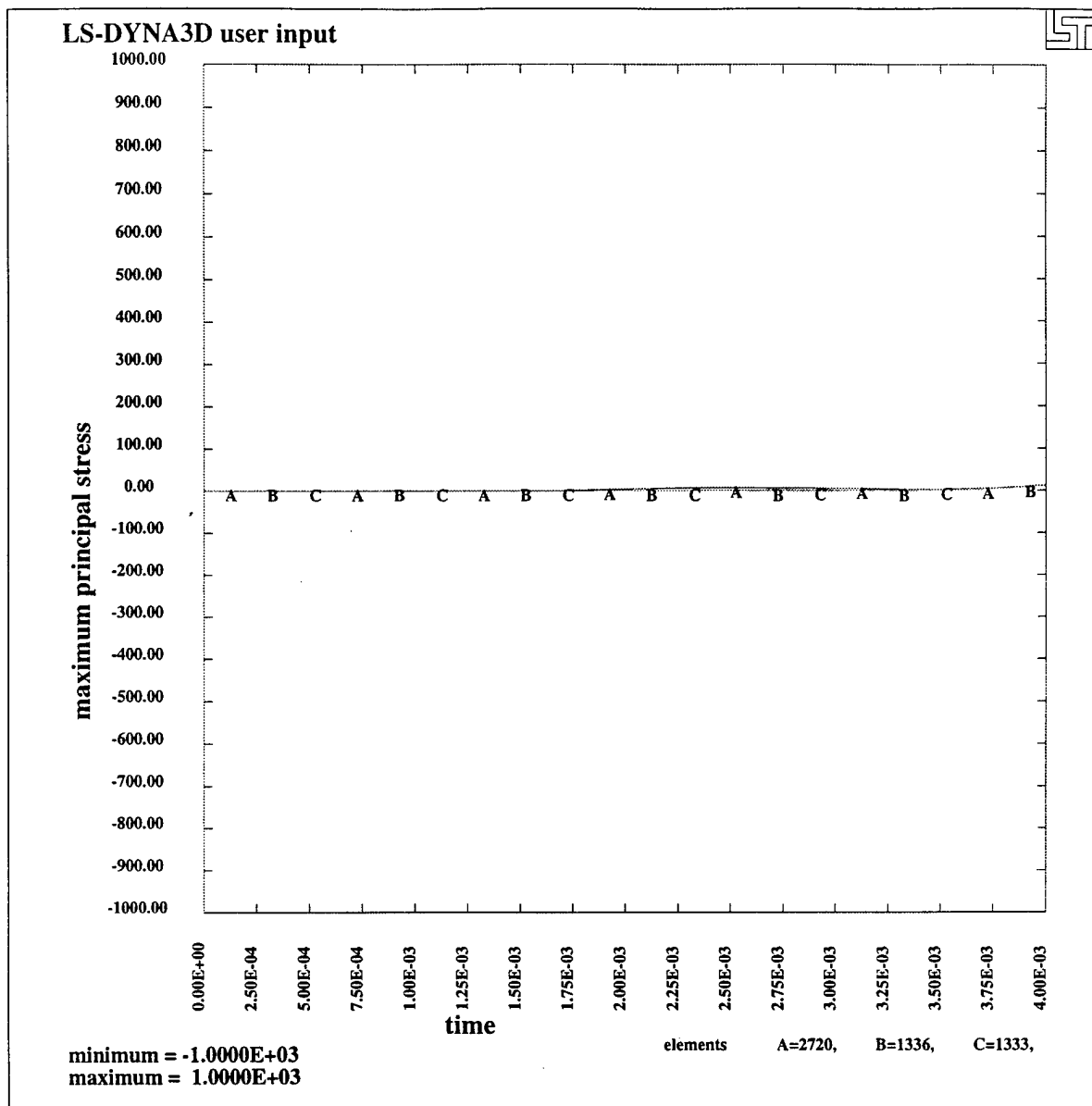


Figure 9-5c: Maximum Principal Stress for representative elements  $\frac{1}{4}$  distance up the tibia.



## 10. CONCLUSIONS

Four materials from the countermine boots were tested to determine the material properties of each: rubber, aluminum honeycomb, steel, and kevlar. Throughout the testing, ASTM standards were adhered to as much as possible. However, due to the limited dimensions of the available material, it was necessary to scale the ASTM standards for some of the specimens.

The testing conducted on the cylindrically-shaped rubber specimens had very consistent results. Several rubber specimens from two different boots behaved in the same manner and proved have the same compressive properties and same Young's modulus throughout their elastic regions.

Testing on the aluminum honeycomb was conducted in three different directions using specimens from two countermine boots and one countermine overboot. Properties were found to be consistent regardless of the source. The failure strength in the vertical direction proved to be over twenty times stronger than that found in either the longitudinal or transverse directions. Similarly, the average Young's modulus found in the vertical direction was more than fourteen and twenty-eight times stronger than those found in the longitudinal and transverse directions, respectively.

The steel used on the upper portion of the shank was proven to be the same Type 302 Stainless Steel used on the bottom of the shank. This was done by a microanalysis of both using Scanning Electron Microscope and an Electron Dispersive X-ray. The lower



steel was then tested and proved to have material properties consistent with those expected of a Type 302 Stainless Steel.

The testing of the kevlar was conducted in both transverse and longitudinal directions. The failure strengths of the specimens were found to be the same in either orientation. The Young's moduli were found to be of the same magnitude but were much greater in the longitudinal direction.

The Finite Element Model, while in its most preliminary form, has given some insight into the nature of the explosion and the forces involved. The time history plots of the stress fields shown in this section would seem to suggest damage and injuries consistent with land mine victims. All of the materials of the boot undergo some amount of permanent deformation and failure.

The next step to improving the model is to examine a longer time period after the blast. To improve the detail of the results an attempt at including the soft tissue of the body should also be included. This tissue may provide additional beneficial damping to the system. However, accounting for the destruction of this tissue and accompanying blood loss will prove difficult at best. It is also considered essential to validate this model with carefully conceived and executed live fire testing.

## LIST OF REFERENCES

1. Office of International Security and Peacekeeping Operations, *Hidden Killers: The Global Landmine Crisis*, US State Dept (1994).
2. Jane's Information Group, *Jane's Military Logistics and Vehicles* (1995).
3. Kinney, Gilbert F and Graham, Kenneth J , *Explosive Shocks in Air*, 2nd Edition, Springer-Verlag (1985).
4. ASTM, *Annual Book of ASTM Standards*, American Society for Testing and Materials, Philadelphia, Pa. Vol. 00.01 (1996).
5. D412-92, *Annual Book of ASTM Standards*, American Society for Testing and Materials, "Standard Test Methods for Vulcanized Rubber and Thermoplastic Rubbers and Thermoplastic Elastomers-Tension," Philadelphia, Pa. Vol. 09.01 (1996).
6. Brown, RP, *Physical Testing of Rubber*, 3<sup>rd</sup> Edition, Chapman and Hall, London (1996).
7. D575-91, *Annual Book of ASTM Standards*, American Society for Testing and Materials, "Standard Test Methods for Rubber Properties in Compression," Philadelphia, Pa. Vol. 09.01 (1996).
8. ASTM E8-96, *Annual Book of ASTM Standards*, American Society for Testing and Materials, "Standard Test Methods for Tension Testing of Metallic Materials," Philadelphia, Pa. Vol. 03.01 (1996).
9. D3039/D3039-95a, *Annual Book of ASTM Standards*, American Society for Testing and Materials, "Standard Test Method for

- Tensile Properties of Polymer Matrix Composites Materials," Philadelphia, Pa. Vol. 15.03 (1996).
10. Gibson, Ronald F., *Principles of Composite Material Mechanics*, McGraw-Hill, Inc., New York, (1994).
  11. Brick, R.M. and Phillips, Arthur, *Structure and Properties of Alloys*, McGraw-Hill Book Company, Inc., New York (1949).
  12. Uguaral, Ansel C. and Fenster, Saul K., *Advanced Strength and Applied Elasticity*, 3<sup>rd</sup> Edition, Prentice Hall, Upper Saddle River, NJ (1995).
  13. Flinn, Richard A. and Trojan, Paul K., *Engineering Materials and Their Applications*, Houghton Mifflin Company, Boston, Ma (1981).
  14. Peckner, Donald, *Handbook of Stainless Steels*, McGraw-Hill Book Co, New York (1977).
  15. Mow, Van C, and Hayes, Wilson C, *Basic Orthopaedic Biomechanics*, Lippencott Raven, (1997).
  16. Nahum, Alan M, and Melvin, John W, *Accidental Injury: Biomechanics and Prevention*, Springer (1993).
  17. ASTM E986-92, *Annual Book of ASTM Standards*, American Society for Testing and Materials, "Standard Practice for Scanning Electron Microscope Performance Characterization," Philadelphia, Pa. Vol. 03.01 (1996).
  18. E-1508-93a, *Annual Book of ASTM Standards*, American Society for Testing and Materials, "Standard Guide for Quantitative Analysis by Energy-Dispersive Spectroscopy," Philadelphia, Pa. Vol. 03.01 (1996).

19. Gray, Allen G., *Source Book on Stainless Steel*, The Periodicals Publication Department, American Society for Metals, Metals Park, Ohio (1977).



APPENDIX A.  
MICROANALYSIS OF THE STEEL SHANK.

### Microanalysis of the steel used in the shank.

In order to most accurately determine the type of steel used as a shell for the aluminum honeycomb filled shank, a Scanning Electron Microscope (SEM) was used in conjunction with an Energy-Dispersive X-ray (EDX) microanalysis. The result of this analysis was that the steel used for both the thin top and thicker wedge-shaped base are both Type 302 Stainless Steel.

The SEM is a more recent innovation in electron microscopy and has proved to be an extremely useful investigative tool. For this analysis, unprepared samples of the steel shank cover were placed in the SEM. (As long as the samples are electrically conductive, no coating or other sample preparation is necessary.) The surface of each sample was scanned with an electron beam. The electrons reflected from the surface are collected and displayed on a cathode ray tube. The features of the surface of the sample appear on the tube (like looking at a TV screen). A complete description of the process used for the SEM is given in ASTM E986-92, [17] Standard Practice for Scanning Electron Microscope Performance Characterization.

The EDX is attached to the SEM as an accessory and allows for qualitative and quantitative analyses of the elemental composition of the small section of each sample being scanned by the electron beam. A brief explanation of how each element is identified by the EDX follows: When the electron beam strikes an element in the sample, electrons are ejected from inner atomic shells to outer shells resulting in ions in the excited state.

When the element relaxes, these ions return to their original shells returning the element to a normal ground state. The most likely case involves a series of transformations in which electrons drop from one shell level to fill a vacancy in an inner shell. The drop from each shell level gives off an amount of energy equal the energy between the two shell levels. The energy is given up in the form of electromagnetic radiation. Knowing the shell level energies of each element, the EDX is able to measure the energy discharged by the sample's atoms and identify which elements are present. The EDX can then display the amount of any elements present in the sample to the user in the form of weight percent. An in-depth description of the procedure used in the EDX analysis is given in ASTM E-1508-93a, [18] Standard Guide for Quantitative Analysis by Energy-Dispersive Spectroscopy.

One limitation of the EDX arises when elements with similar atomic numbers are present. The result can often be that the two elements will appear in the same "peak" on the screen of the EDX. This is a result in the similar amounts of energy between shell levels. In order to separate the two elements, a method of Gaussian deconvolution is used to separate the overlapping peaks.

An EDX microanalysis of the two type of steel samples was used along with the ASM Source Book on Stainless Steels [19] to identify the type of steel used in the shank.

Initial analysis proved to be accurate enough to declare the thin top of the shank and the thicker bottom of the shank were made of a common iron-chromium-nickel steel; that is, a type 300 series steel. Both samples possessed a Chromium content within



1.8 percent of each other and Nickel composition within 1.1 percent. However, in order to most accurately determine the AISI type of steel, both of the samples were reanalyzed. This analysis requested that the amount of Manganese be determined and utilized Gaussian deconvolution. This was done because the atomic numbers for Chromium, Manganese, Iron, and Nickel are 24, 25, 26, and 28, respectively. The results indicated weight percentages as follows: 71% Iron, 19% Chromium, 8% Nickel, and 2% Manganese. These values were then compared to the AISI standards for different types of steel and it was found that they were consistent with AISI Type 302 stainless steel [14]. Results are indicated in Table A-1.

Table A-1 Comparison of elemental content.

	% Cr	% Ni	% Mn
<i>AISI Type 302</i>	<i>17-19</i>	<i>8-10</i>	<i>2</i>
Thin Sample	18.96	7.83	1.9
Thick Sample	20.67	7.62	1.79

APPENDIX B.

STRESS VS STRAIN CURVES OF RUBBER SPECIMENS.

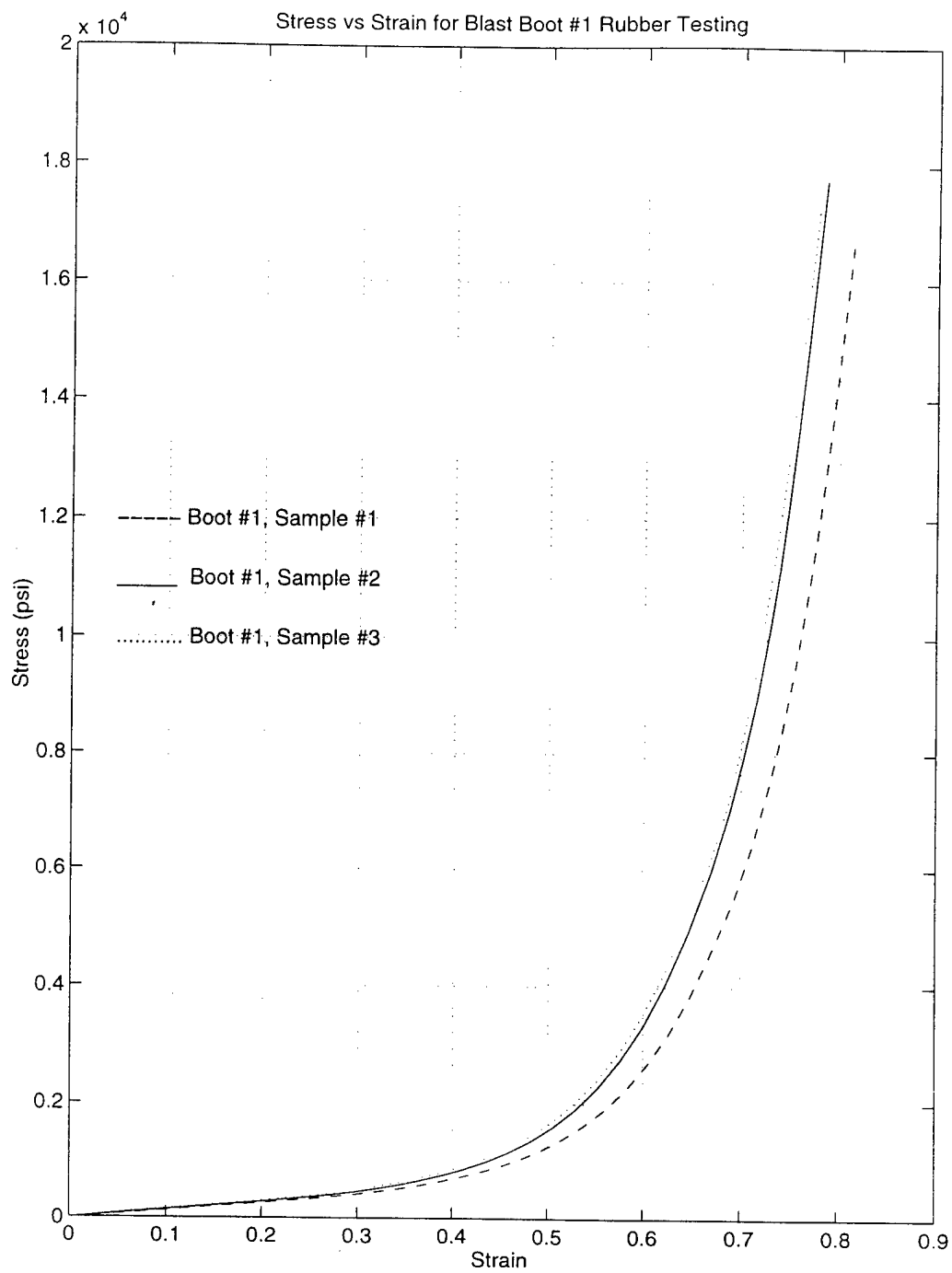


Figure B-1.

010

Figure B-1 compares stress vs strain curves for three rubber samples from the same boot (Boot #1).

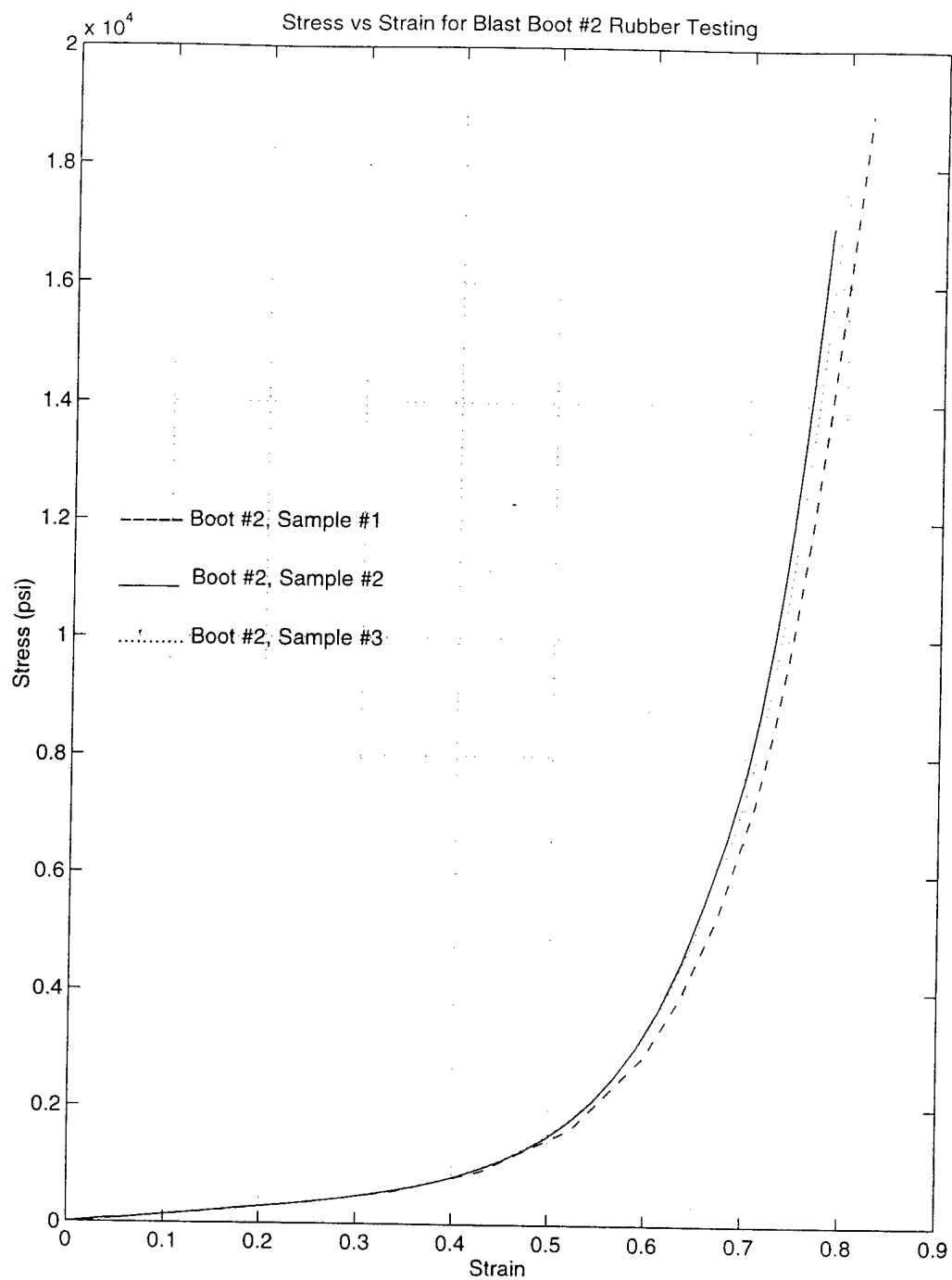


Figure B-2.

Figure B-2 compares stress vs strain curves for three rubber samples from the same boot (Boot #2).

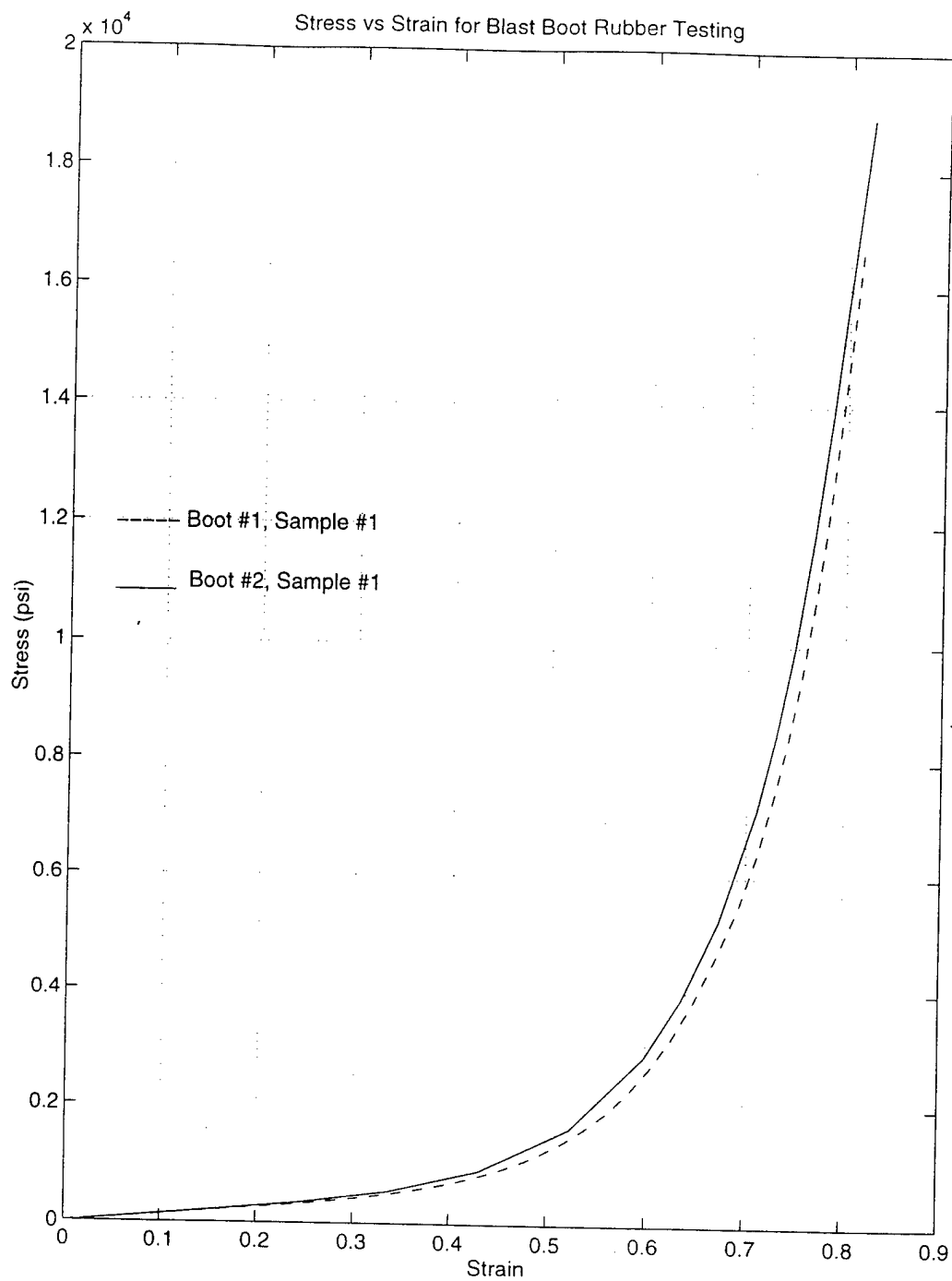


Figure B-3.

Figure B-3 compares stress vs strain curves for two rubber samples (Samples #1) from the two different boots.

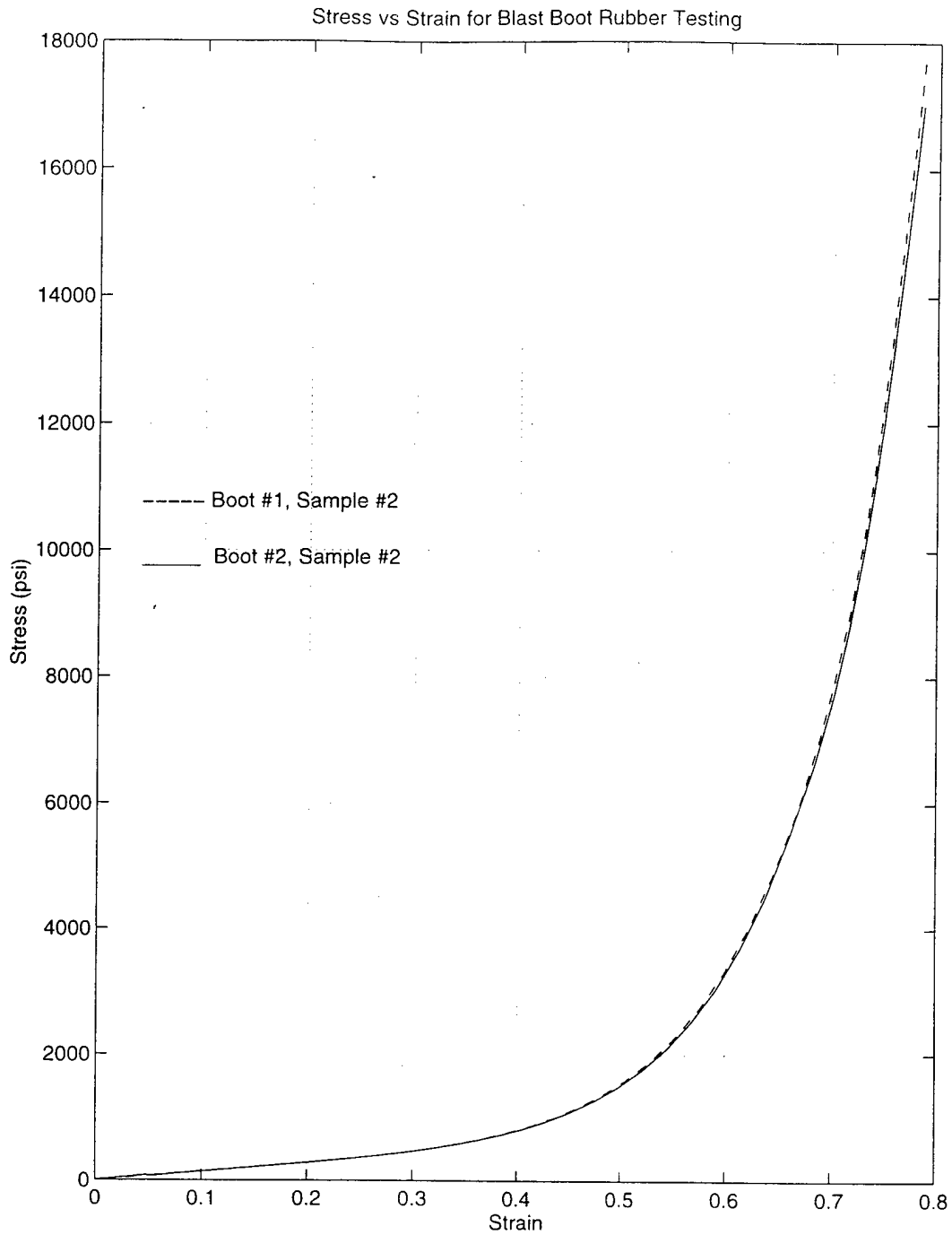


Figure B-4.

Figure B-4 compares stress vs strain curves for two rubber samples (Samples #2) from two different boots.

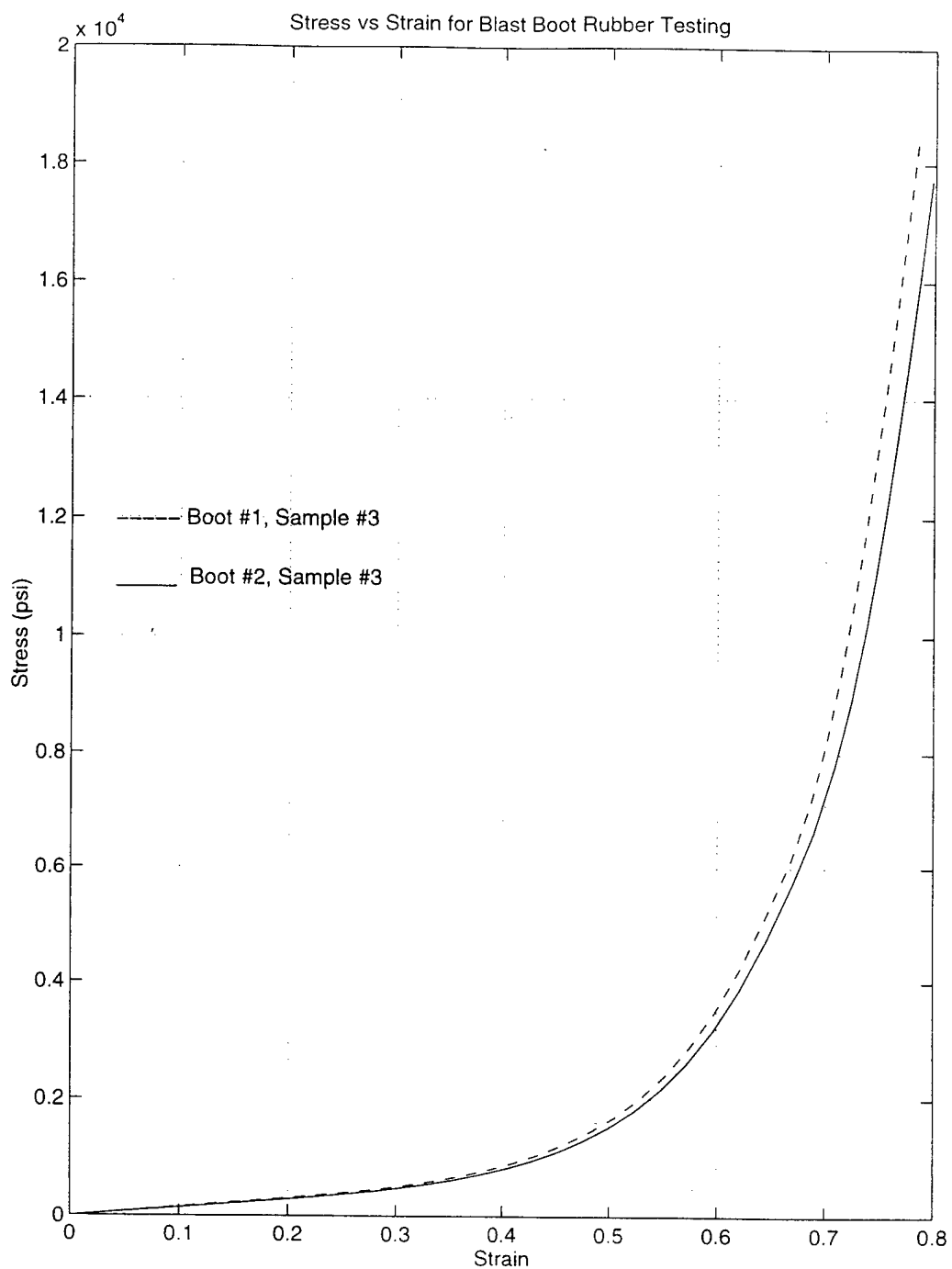


Figure B-5.

Figure B-5 compares stress vs strain curves for two rubber samples (Samples #3) from two different boots.

APPENDIX C.

STRESS VS STRAIN CURVES OF HONEYCOMB SPECIMENS.



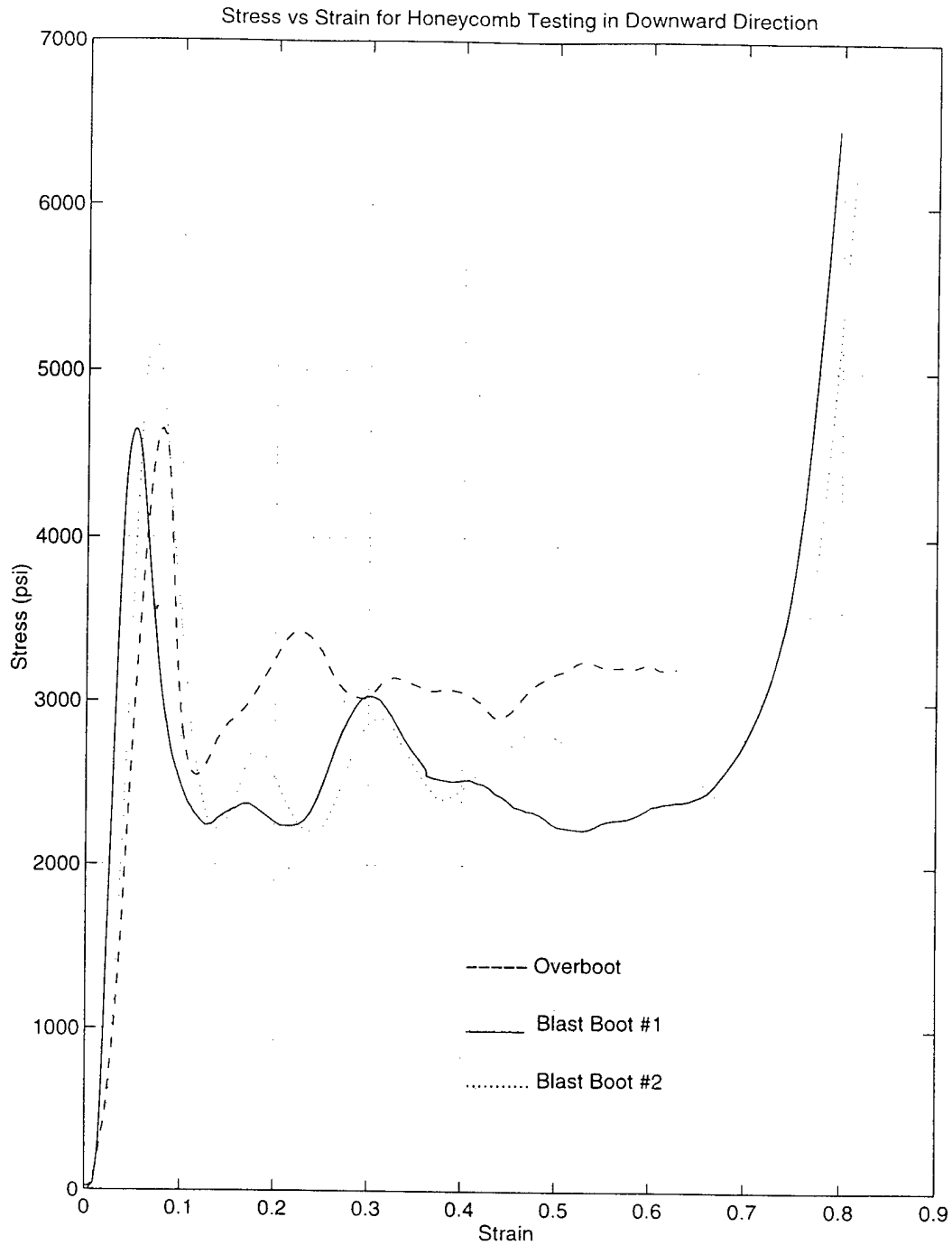


Figure C-1.

Figure C-1 compares stress vs strain curves for three honeycomb samples compressed in the downward direction shows consistent behavior for all three specimens.

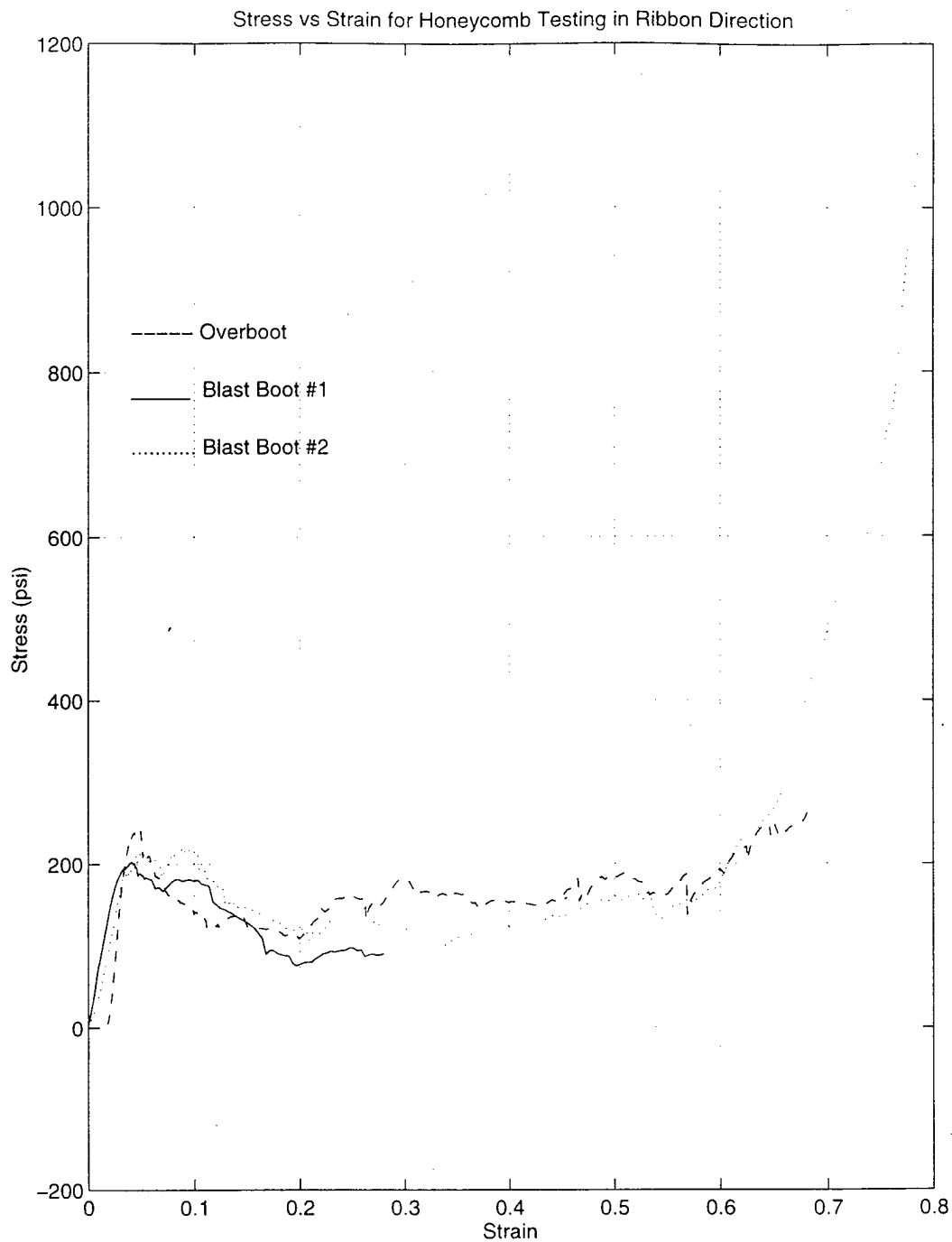


Figure C-2.

Figure C-2 compares stress vs strain curves for three honeycomb samples compressed in the longitudinal direction shows consistent behavior for all three specimens.

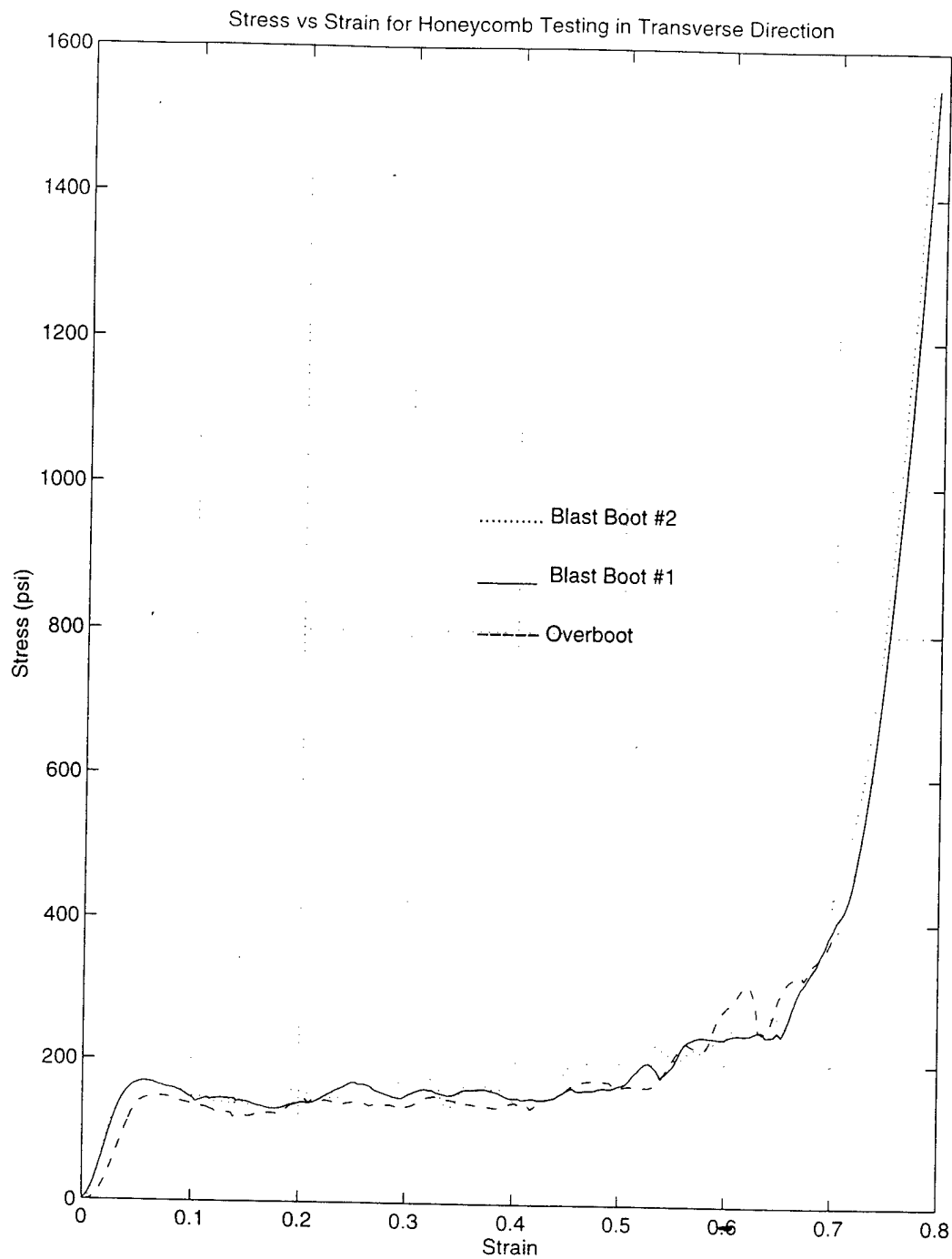


Figure C-3.

Figure C-3 compares stress vs strain curves for three honeycomb samples compressed in the transverse direction shows very similar behavior throughout the compression.

APPENDIX D.

STRESS VS STRAIN CURVES OF STEEL SPECIMENS.

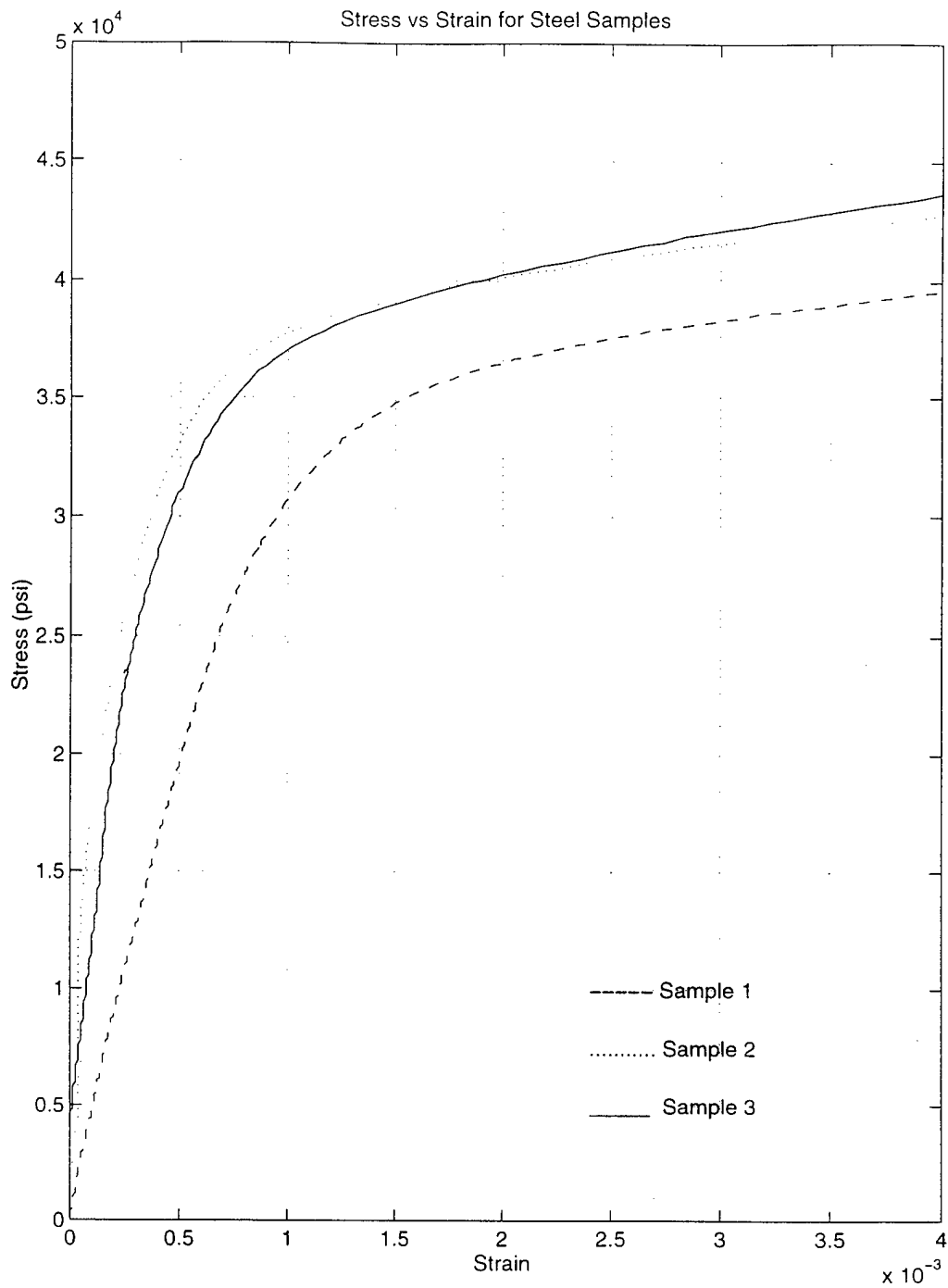


Figure D-1.

Figure D-1 compares stress vs strain curves for three steel samples. The graph shows the closeness of yield strengths and very similar Young's moduli for Samples 2 and 3.

APPENDIX E.

STRESS VS STRAIN CURVES OF KEVLAR SPECIMENS.

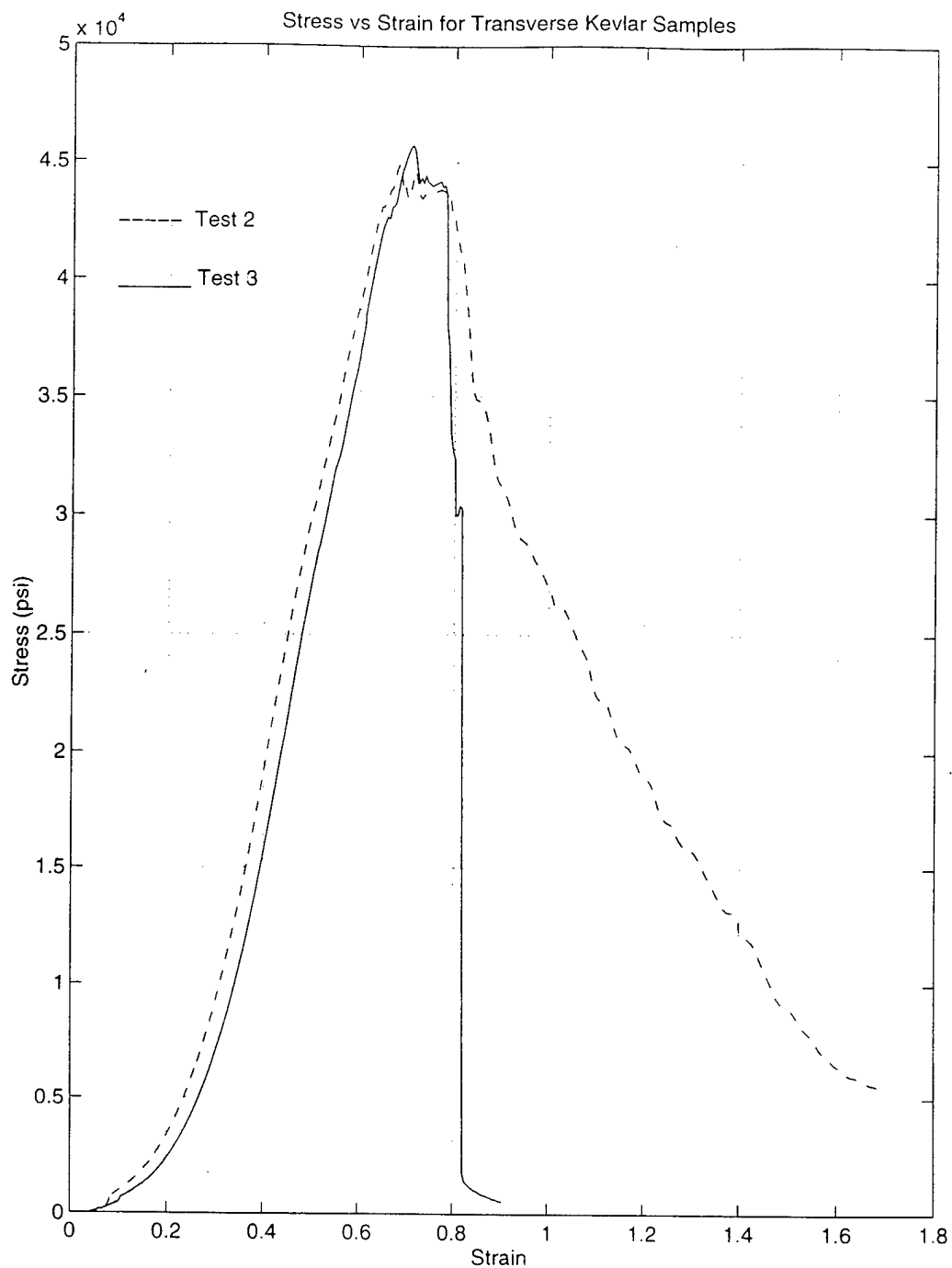


Figure E-1.

Figure E-1 compares stress vs strain curves for two of the transverse kevlar samples shows very close Young's moduli and failure strengths.

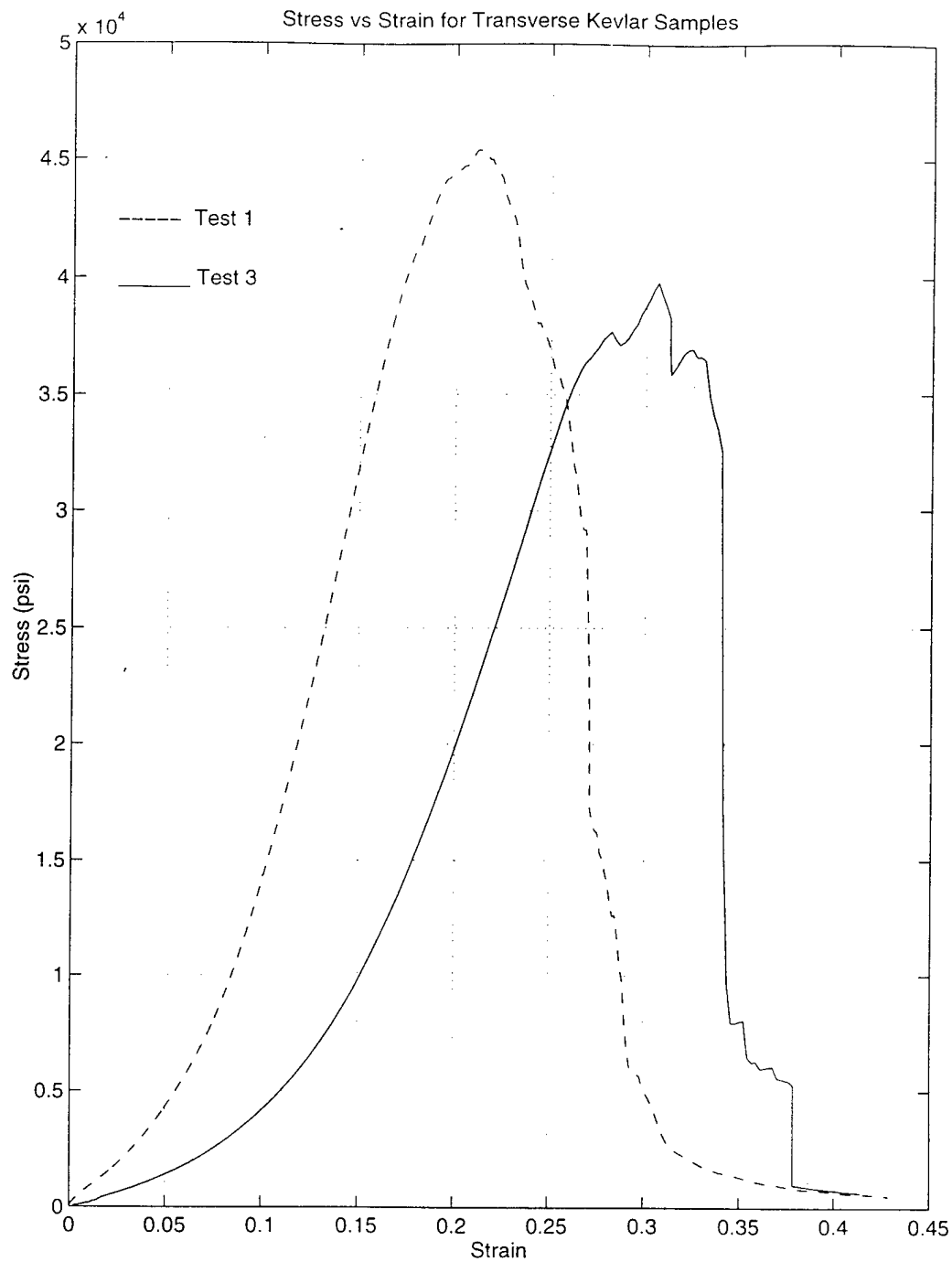


Figure E-2.

Figure E-2 compares stress vs strain curves for two longitudinal kevlar samples shows relatively close failure strengths.





APPENDIX F.

ELEMENT LOCATIONS IN THE FINITE ELEMENT MODEL.

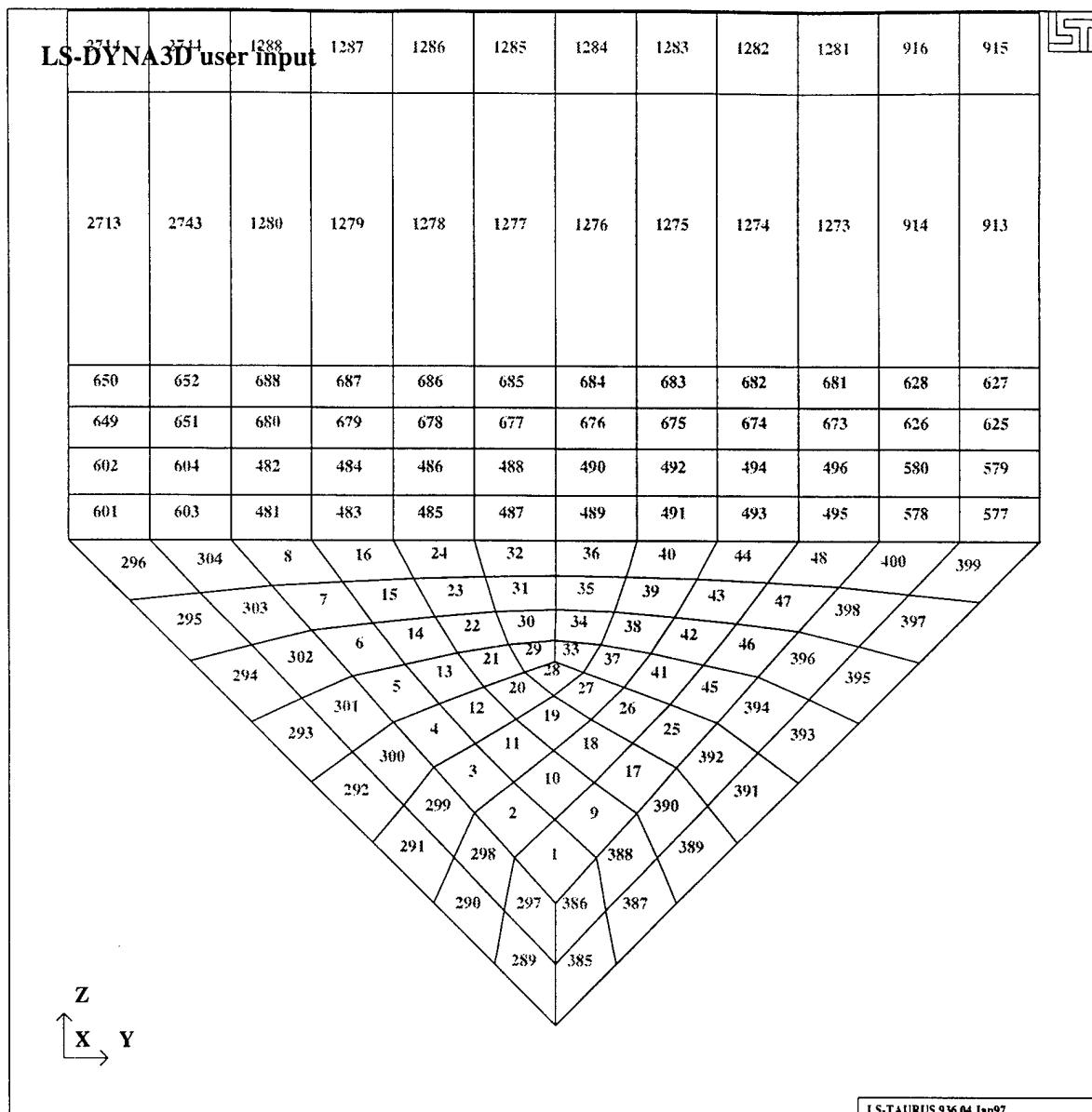


Figure F-1.

Figure F-1 shows a cross-sectional view of the entire finite element model with element numbers identified.

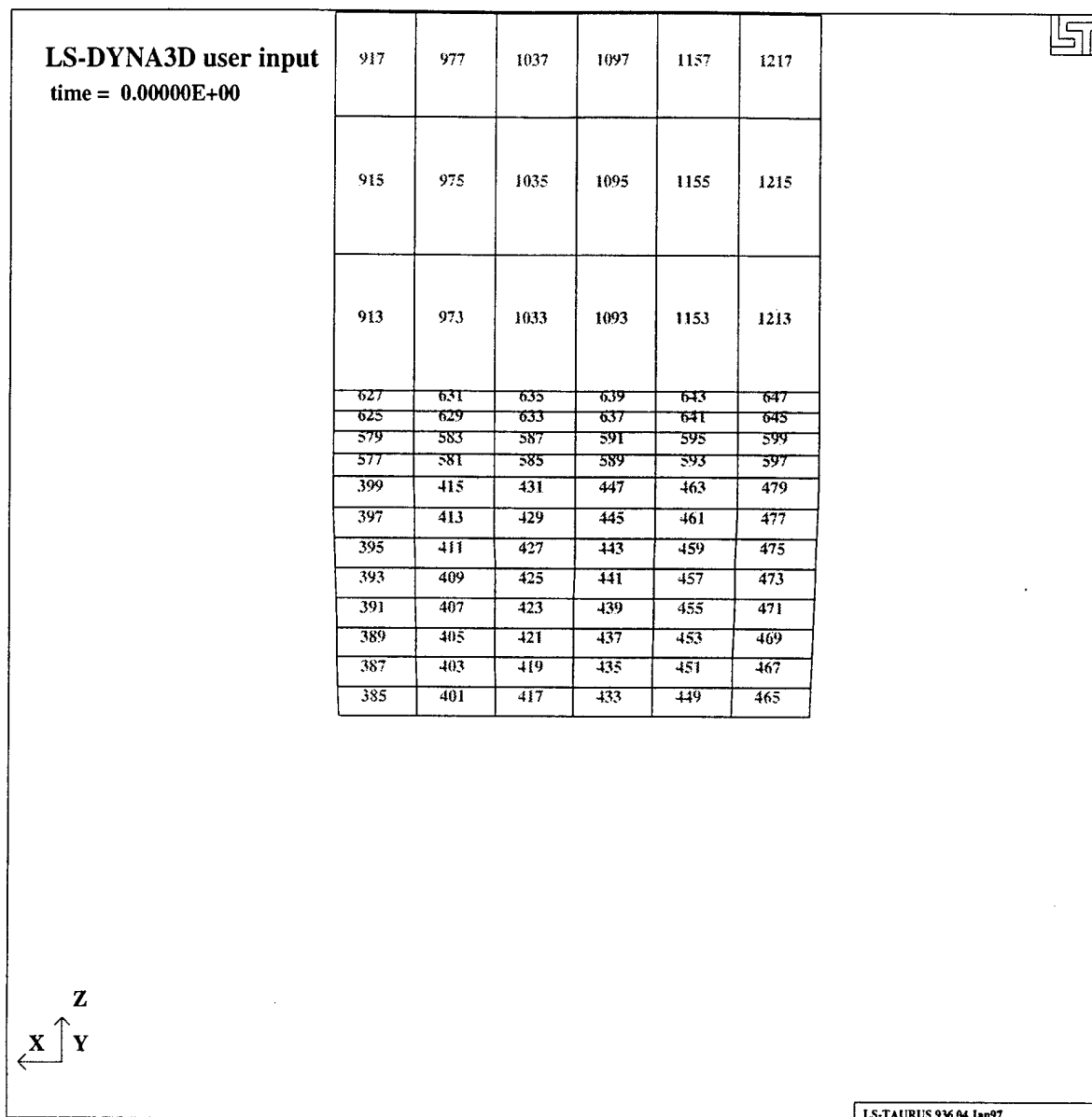


Figure F-2.

Figure F-2 shows a side view of the entire finite element model with element numbers identified.

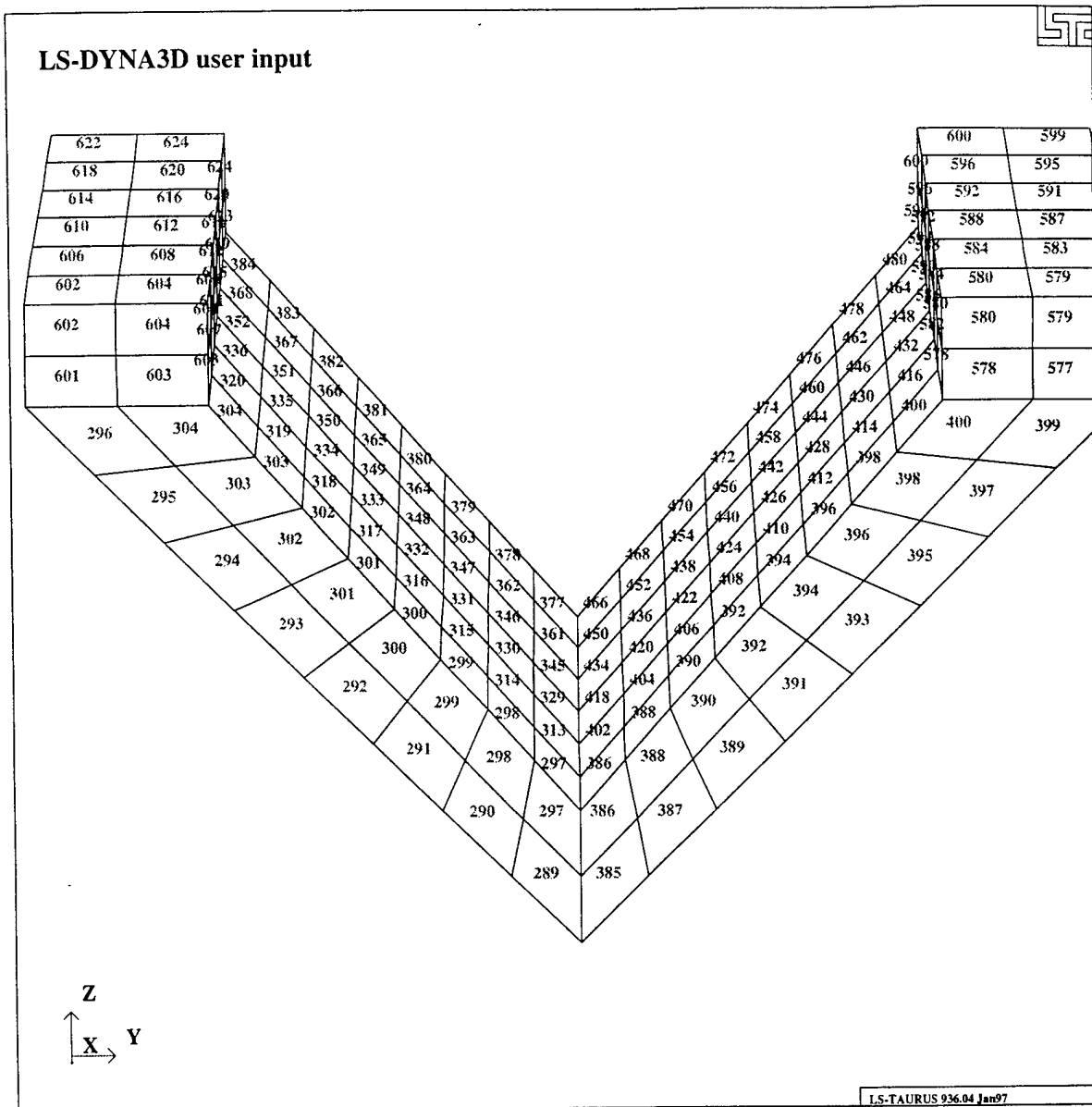
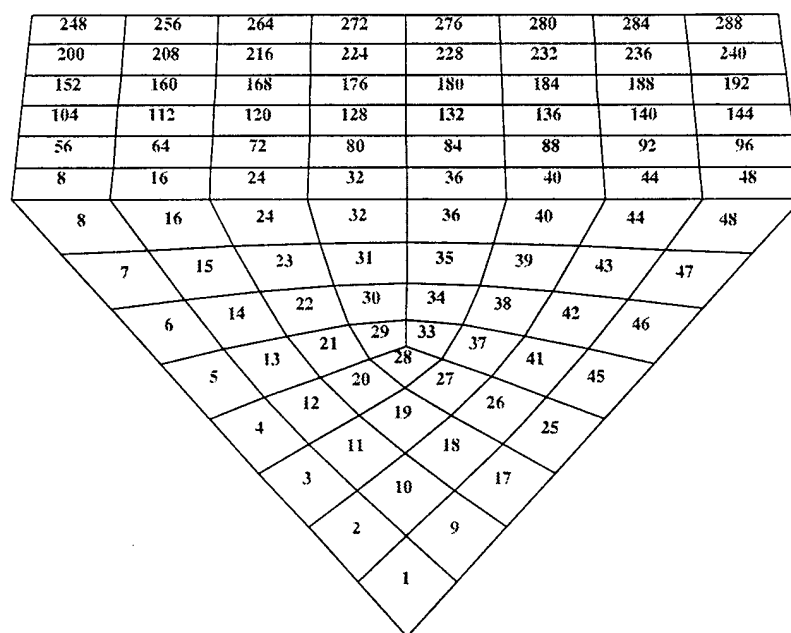


Figure F-3.

Figure F-3 shows the rubber model with element numbers identified.

# LS-DYNA3D user input



LS-TAURUS 936.04 Jan97

Figure F-4 shows the honeycomb model with element numbers identified.

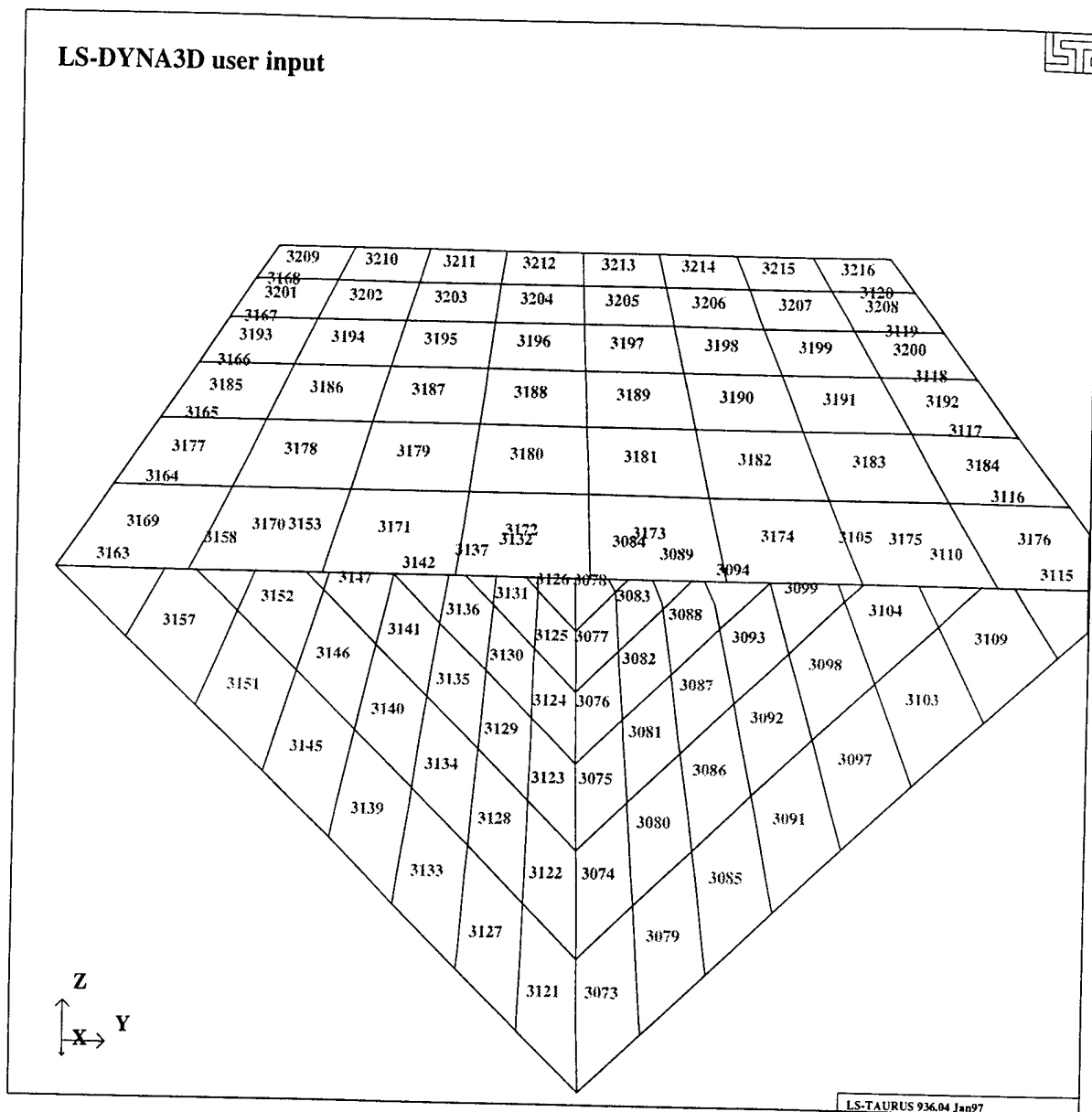


Figure F-5.

Figure F-5 shows the stainless steel shell model with element numbers identified.

# LS-DYNA3D user input

562	564	566	568	570	572	574	576
546	548	550	552	554	556	558	560
530	532	534	536	538	540	542	544
514	516	518	520	522	524	526	528
498	500	502	504	506	508	510	512
482	484	486	488	490	492	494	496
482	484	486	488	490	492	494	496
481	483	485	487	489	491	493	495



LS-TAURUS 936.04 Jan97

Figure F-6.

Figure F-6 shows the kevlar liner model with element numbers identified.



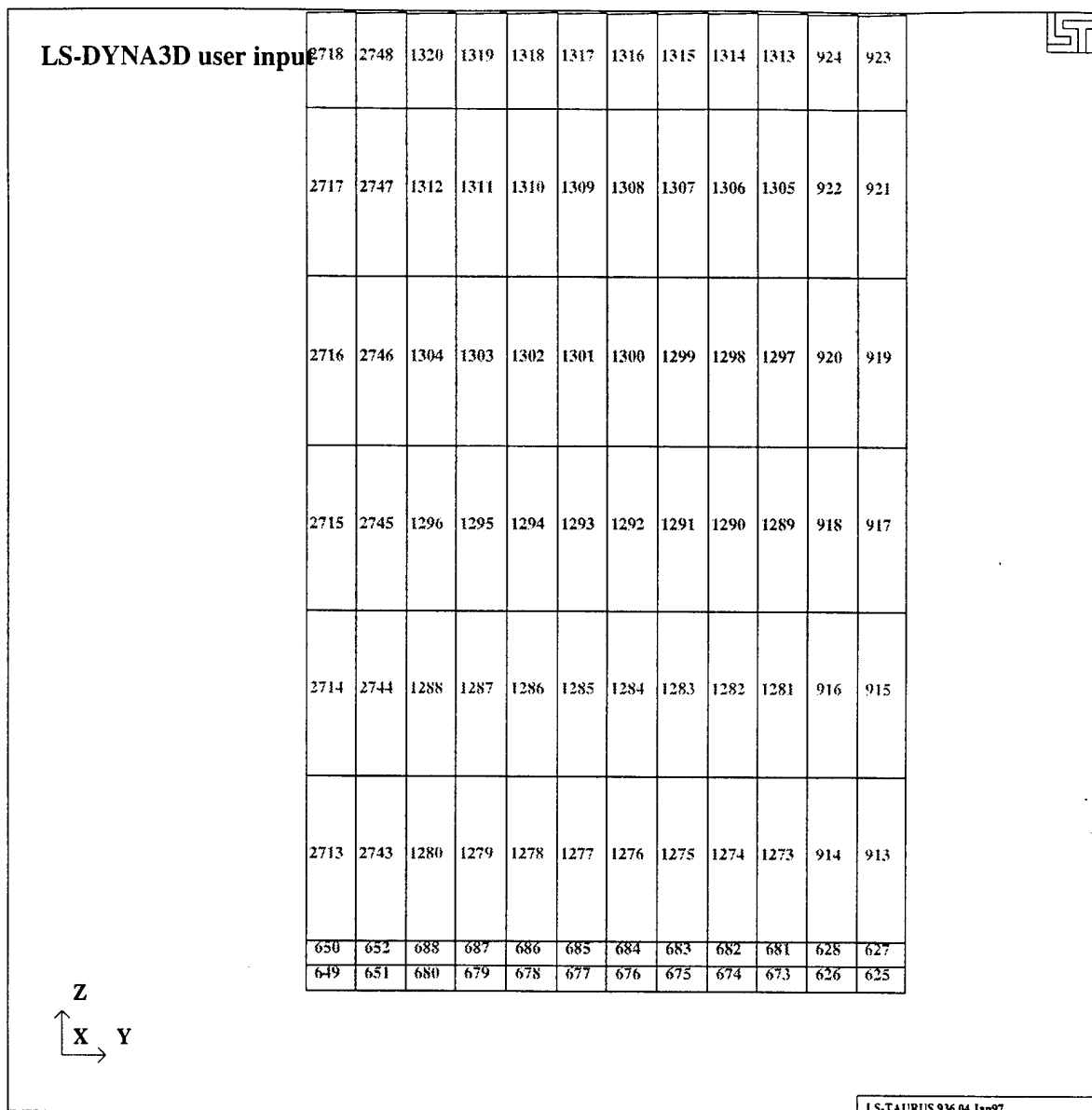


Figure F-7.

Figure F-7 shows the lower portion of the bone model with element numbers identified.

# INITIAL DESTRIUTION LIST

	No. of Copies
1. Defense Technology Information Center Cameron Station Alexandria, VA 22304-6145	2
2. Library, Code 52 Naval Postgraduate School Monterey, California 93943	2
3. Professor Young W. Kwon, Code ME/Kw Naval Postgraduate School Monterey, California 93943	2
4. LT Quinten King, Code ME/Sect 62 Naval Postgraduate School Monterey, California 93943	1
5. CPT Richard C. Muschek, Code ME/Sect 62 Naval Postgraduate School Monterey, California 93943	1
6. Mr. Douglas Davis Program Manager Combat Support and Logistics Equipment Marine Corps Systems Command Quantico, Virginia 22134-5010	1
7. Research Office, Code 09 Naval Postgraduate School Monterey, California 93943	1